AGU100 ADVANCING EARTH AND SPACE SCIENCE

JGR

Journal of Geophysical Research: Solid Earth

RESEARCH ARTICLE

10.1029/2018JB016060

S Velocity Model of East Asia From a Cluster Analysis of Localized Dispersion

M. Witek[1], S. van der Lee[2], T.-S. Kang[3], S.-J. Chang[1], J. Ning[4], and S. Ning[4]

[1]Division of Geology and Geophysics, Kangwon National University, Chuncheon, South Korea, [2]Department of Earth and Planetary Sciences, Northwestern University, Evanston, IL, USA, [3]Department of Earth and Environmental Sciences, Pukyong National University, Busan, South Korea, [4]School of Earth and Space Sciences, Peking University, Beijing, China

Key Points:
- We collected and processed 1 year of ambient seismic noise at over 1,000 stations in East Asia
- Cluster analysis on the localized dispersion model reveals large-scale tectonic provinces
- The cluster centroid models were used to create an improved 3-D *S* velocity model of East Asia

Supporting Information:
- Supporting Information S1

Correspondence to:
M. Witek,
mwitek@kangwon.ac.kr

Citation:
Witek, M., van der Lee, S., Kang, T.-S., Chang, S.-J., Ning, J., & Ning, S. (2018). *S* velocity model of East Asia from a cluster analysis of localized dispersion. *Journal of Geophysical Research Solid Earth*, *123*. https://doi.org/10.1029/2018JB016060

Received 7 MAY 2018
Accepted 4 OCT 2018
Accepted article online 10 OCT 2018

Abstract We measured Rayleigh wave group velocity dispersion curves from station pair cross correlations of continuous broadband data from 1,082 seismic stations in regional networks across China, Korea, and Japan. The dispersion curves are localized in the period range 6–40 s to produce group velocity maps, which we then combine with group velocity data in the period range 50–133 s from the global dispersion model of Ma et al. (2014, https://doi.org/10.1093/gji/ggu246). Cluster analysis performed on the local dispersion curves reveals distinct tectonic regions and provides a new way of estimating the number of regions needed to describe a surface wave dispersion data set. We inverted the centroid dispersion curves corresponding to each cluster for a new set of reference models. We used a combination of teleseismic receiver functions and Moho depths from the LITHO1.0 model to create a 3-D Moho depth reference model and then constructed a 3-D *S* velocity model by jointly inverting group velocities with localized phase velocities in the period range 28.57–200 s, also from Ma et al. (2014, https://doi.org/10.1093/gji/ggu246). The cluster analysis and comparisons with other regional models provide evidence for a broad region of deformed lithosphere in East Asia. We image high velocities in the Yangtze and Ordos cratons and low velocities underneath the East Sea (Sea of Japan), and we find that a low-velocity zone in the midcrust is appropriate for Tibet. The model we present is intended as an alternative reference model that fits a broader range of periods to be used for further studies of regional geophysical phenomena.

1. Introduction

East Asia is a complex framework of stable cratonic blocks and orogenic belts, whose origins and mechanisms of formation remain debated today. These blocks are bounded by suture zones and major faults representing the locations of former oceanic basins (Metcalfe, 2006). The North China craton (NCC), also known as the Sino-Korean craton, can be divided into distinct western and eastern portions, separated by the Trans-North China orogen (Kusky & Li, 2003; Y.-F. Zheng et al., 2013). The NCC has a thick (≥200 km) lithosphere in its western part (Ordos) but progressively thins toward its eastern margin. Geochemical observations indicate that the thinning of the eastern NCC lithosphere may have been initiated by the subduction of the Pacific plate (Z. Xu et al., 2012; Zhang et al., 2009). However, the exact mechanism for the lithospheric destruction, whether by gradual erosion or by delamination, is still a debated topic. The NCC is bound to the south by the Qinling-Dabie-Sulu orogenic belt. The Sulu orogeny is separated from the Dabie orogeny by the Tan-Lu fault, which is the largest strike-slip fault in East Asia. There is some evidence that the Imjingang Belt in Korea is an extension of the Qinling-Dabie-Sulu collisional belt (Kwon et al., 2009; Lee et al., 2000; Ree et al., 1996); however, whether the whole of the Korean Peninsula belongs to the NCC, or whether the southern portion is an extension of the Yangtze craton or the Cathaysia block, is an area of active research (S.-J. Chang & Baag, 2007; K.-H. Chang & Zhao, 2012; Yu et al., 2012).

The South China block (SCB) is composed of the Yangtze craton in the northwest and the Cathaysia block to the southeast. These two terranes collided along the Jiangnan orogen, and while most researchers believe the timing of this event was in the Neoproterozoic, the exact timing and mechanism is debated (G. Zhao & Cawood, 2012; Y.-F. Zheng et al., 2013). The Yangtze craton developed independently of the NCC during the Paleoproterozoic (Y.-B. Wu et al., 2009). Geochemical evidence suggests that the Yangtze craton was formed by circa 2.0 Ga via an amalgamation of microblocks (Y. Wu et al., 2012; G. Zhao & Cawood, 2012; Y. Zheng & Zhang, 2007; Y.-F. Zheng et al., 2013). On the other hand, it is unknown whether the Cathaysia block was a stable cratonic region or whether it formed by various accretion events (Y.-F. Zheng et al., 2013).

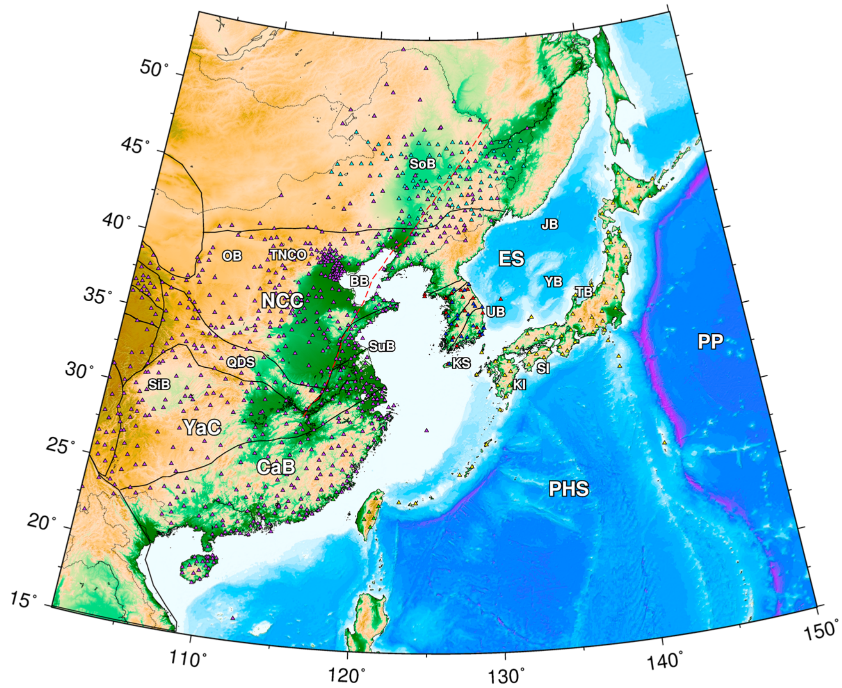

Figure 1. Broadband seismometer stations used in this study: (purple) CRSN, (yellow) F-net, (green) BATS, (cyan) NECESSarray, (blue) Korea Institute of Geoscience and Mineral Resources, and (red) Korea Meteorological Administration. Labels indicate locations of geologic units: ES = East Sea; UB = Ulleung basin; YB = Yamato basin; JB = Japan basin; TB = Toyama basin; KS = Korea Strait; KI = Kyushu Island; SI = Shikoku Island; SoB = Songliao basin; BB = Bohai Bay basin; SuB = Subei Yellow Sea basin; SiB = Sichuan basin; NCC = North China craton; OB = Ordos block; YaC = Yangtze craton; CaB = Cathaysia block; TNCO = Trans-North China orogen; QDS = Qingling-Dabie-Sulu belt; PHS = Philippine Sea plate; PP = Pacific plate. Red dashed line delineates the Tan-Lu fault.

Prior to the Oligocene, Japan lay at the eastern edge of the Eurasian continent, and by the mid-Miocene, Japan was actively rifting away, leading to the formation of the East Sea, a complex continent-ocean back-arc basin. Its development has been constrained by the interactions of the Eurasian, Pacific, and Philippine Sea plates. The two oceanic plates are subducting directly underneath the Eurasian plate in a WNW direction, with the Pacific plate moving at 9–11 cm/year and the Philippine Sea plate moving at 3–6 cm/year (DeMets et al., 2010; Maruyama & Seno, 1986; Matsubara & Seno, 1980; Northrup et al., 1995; Seno & Maruyama, 1984). The mechanism of basin formation has been suggested to follow either a fan-shaped model or a pull-apart model, and studies of the timing show that spreading must have happened during a period of 21–15 Ma, but the exact details are still under debate (Jolivet et al., 1995; Kano et al., 2007; Lallemand & Jolivet, 1986; Nohda, 2009; Otofuji et al., 1985, 1991).

In order to investigate the tectonic features, many regional geophysical studies have been carried out in East Asia. Due to the sparsity of seismometer station coverage in the region, among the first were regional and teleseismic surface wave studies to examine the crustal and uppermost mantle structure of Tibet (e.g., Bird & Toksöz, 1977; Chen & Molnar, 1981; Gupta & Narain, 1967; Jobert et al., 1985; Pines et al., 1980; Romanowicz, 1982). Since the establishment of dense broadband digital seismometer networks, studies with increasing amounts of data and resolution have been carried out (e.g., Acton et al., 2010; Curtis et al., 1998; Feng & An, 2010; Huang et al., 2003, 2009; Lebedev & Nolet, 2003; Legendre et al., 2014; Ritzwoller & Levshin, 1998; Villaseõr et al., 2001; F. T. Wu et al., 1997). However, earthquake-based surface wave tomography has its resolution determined by the time and spatial distribution of earthquakes, which occur mainly at plate boundaries. Tomographic studies using ambient seismic noise circumvent this issue because measurements are made along interstation paths, which is useful in relatively aseismic regions such as continental interiors. While the utility of ambient seismic noise has been known since Aki (1957), it was only after the availability of dense seismometer arrays with digital instrumentation and the work of Lobkis and Weaver (2001) that group and phase velocity measurements from ambient noise cross correlations became feasible (Shapiro, 2005).

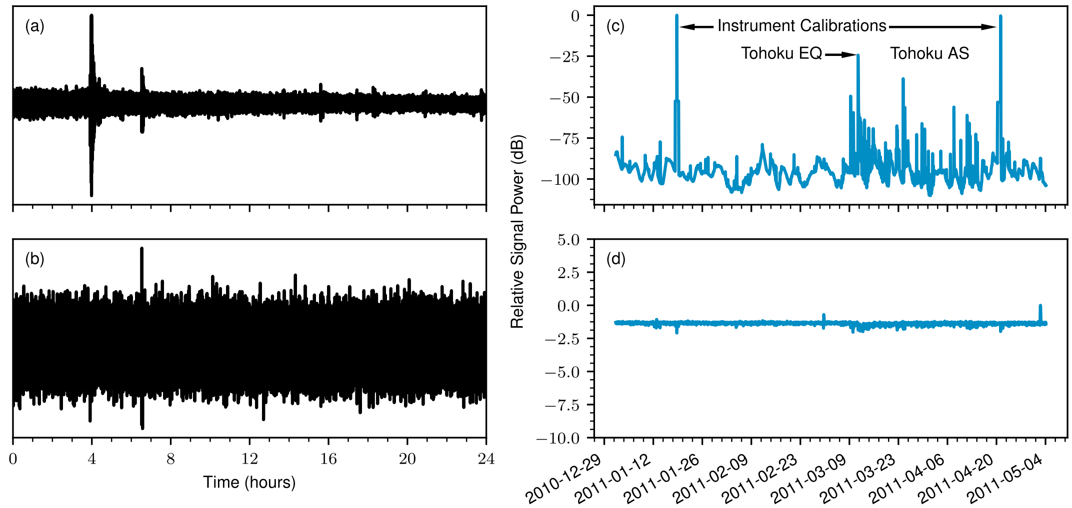

Figure 2. (a) Comparison of a 24-hr time series record before and (b) after application of the FTN method for station DAG2 in Korea, on 16 March 2011, starting at 00:00:00 UTC. (c) Comparison of the average power in a 4-month period for the Korean station DAG2 before applying FTN, and (d) after FTN. The units are in decibels relative to the maximum value in each plot. Denoted by arrows are spikes in the signal power caused by instrument calibrations and the 11 March 2011 Tohoku earthquake. The Tohoku aftershock sequence is also labeled. FTN = frequency-time normalization.

Ambient noise studies of East Asia are now numerous (e.g., Cho et al., 2007; Choi et al., 2009; Fang et al., 2010; Kang & Shin, 2006; H. Li et al., 2009; W. Shen et al., 2016; Yang et al., 2010; Yao et al., 2006, 2008; Yao & van der Hilst, 2009; Yang et al., 2012; Y. Zheng et al., 2011; S. Zheng et al., 2008; Zhou et al., 2012).

Cluster analysis has been applied in geophysical studies going back decades (e.g., Aminzadeh & Chatterjee, 1984; Davis & Frohlich, 1991) and has been used to explore nonuniqueness in tomographic models (e.g., Mikhailov et al., 2003; Vasco et al., 1996), to study earthquake locations and aftershock sequences (e.g., Davis & Frohlich, 1991; Lin et al., 2007; Shearer, 2005; Zaliapin et al., 2008), to improve measurements of body wave traveltimes (Houser et al., 2008) and Rayleigh and Love wave group and phase velocities (Ma & Masters, 2014; Ma et al., 2014), and to explore and compare global tomographic models (Lekic & Romanowicz, 2011; Lekic et al., 2012). In this study, we expand on the work of Witek et al. (2014), who created a Rayleigh wave group velocity dispersion model of Korea and Japan, and create a dispersion model for East Asia derived from 1-year stacks of ambient noise cross correlations in the period range 6–40 s. We combine our model with the earthquake-based global dispersion model of Ma et al. (2014) and perform a cluster analysis of the localized dispersion curves that results in a tectonic regionalization similar to Lekic and Romanowicz (2011). We show that we can create a set of 1-D reference models by first inverting the cluster centroid dispersion curves. These new reference models are then used in a subsequent inversion for 3-D shear wave velocity structure that produces a higher level of data fit than an inversion using a single 1-D reference model for the whole region.

2. Data Processing

2.1. Daily Record Processing

We processed continuous waveform vertical-component data from 1,082 broadband seismometers across regional networks in China, Taiwan, Korea, and Japan for the year 2011 (Figure 1). The average and median interstation distance is around 1,500 km, while interstation orientations are primarily in the NE-SW direction. Each station's data were converted to units of ground velocity, decimated to 1 Hz, and assembled into daily 24-hr sections with their linear trend removed and edges tapered, and were normalized and equalized according to the method of frequency-time normalization (FTN) described by Y. Shen et al. (2012) and also used by Ekström et al. (2009) and Nolet (1990). In our application of the method, we applied a series of overlapping Gaussian filters, in the frequency range 0.01–0.4 Hz. The bandwidth we used was one fourth the low-frequency limit, or 0.0025 Hz. Each band passed time series is divided by its envelope, and in the final step all equalized, filtered time series are summed resulting in a frequency-time normalized waveform (Figure 2). To further illustrate the effect of this normalization, we compute the average signal power in 1-hr intervals for data from Korean station DAG2, and we compare it before and after normalization (Figure 2). We define the

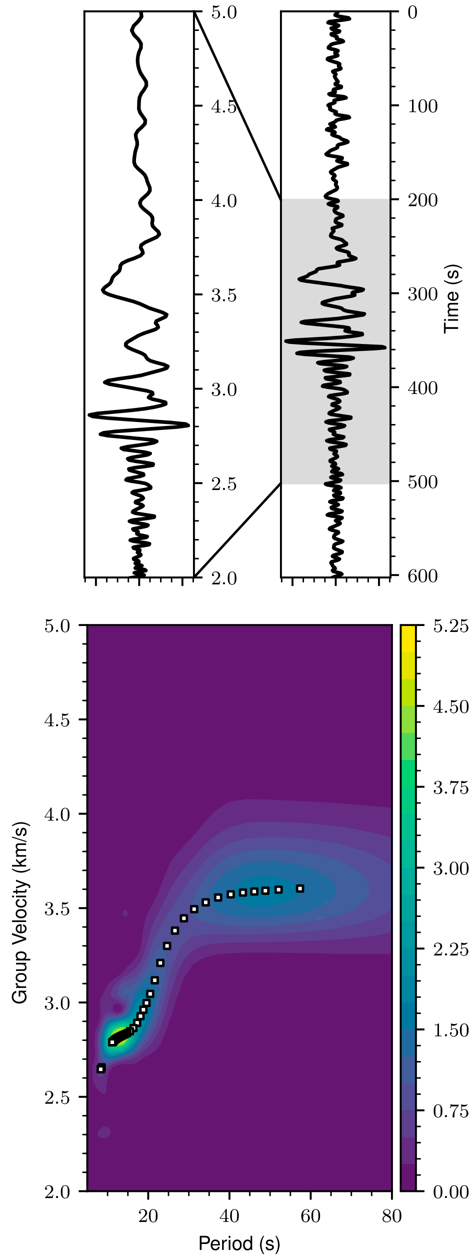

Figure 3. (left) A spectrogram from a 1-year stack of cross correlations between Chinese station NIB and Japanese F-net station INN, with an interstation distance of roughly 1,000 km. Colors represent envelope values, and white squares show automatic dispersion curve measurements. (middle) The 1-year cross-correlation stack for this pair of stations, with group velocity on the *y* axis. (right) The same cross-correlation stack with time on the *y* axis. The light gray region shows the signal window.

average power in an arbitrary time interval ΔT as

$$P(t_0) = \frac{1}{\Delta T} \int_{t_0 - \frac{\Delta T}{2}}^{t_0 + \frac{\Delta T}{2}} s^2(t) \mathrm{d}t, \tag{1}$$

where t_0 is the center of the window and $s(t)$ is the signal. Figure 2 shows that the FTN method indeed produces waveforms with relatively constant power.

2.2. Cross Correlation and Dispersion Curve Measurement

After the FTN procedure, every station pair has their respective 24-hr FTN time series cross-correlated and stacked, for a total of 584,821 one-year cross-correlation stacks. For quality control, we measure the coherency of the positive and negative lag time sides of the cross-correlation stacks. If the two sides are incoherent, we find that calculating the so-called *symmetric* signal, or the average of the two sides, can cause destructive interference and decrease the signal-to-noise ratio (SNR), even if one side of the cross correlation is well retrieved. Therefore, to increase the amount of useful measurements, if the coherency is greater than or equal to an empirically chosen threshold of 0.5, we take the average of the positive and negative sides to measure the group velocity. If the coherency is less than 0.5, we measure the dispersion curve on the side with the higher SNR instead of taking the average of both sides. During group time measurement, we discard any measurement with an SNR less than 10. We define the SNR as the ratio of the maximum amplitude in a signal window to the root-mean-square (RMS) value in a 500-s long noise window 2,000 s after the end of the signal window. The signal window is defined by the arrival times for a surface wave traveling between 2 and 5 km/s. Using a phase velocity reference curve from the *ak135* model, measurements for which the interstation distance is less than three wavelengths are also not used during the surface wave tomography.

To measure group velocity dispersion curves, we begin by creating an *analytic* signal and follow the multiple filter technique to create frequency-time analysis diagrams (Dziewonski et al., 1969; Levshin et al., 1972, 1992). We filter the signal in the frequency domain using Gaussian filters at a series of center frequencies with filter widths determined using a reference dispersion curve from the *ak135* model and the method outlined in Cara (1973), in which the filter width is calculated by optimizing the time resolution of a filtered signal. After transformation back to the time domain, the group time of the fundamental mode Rayleigh wave at a particular center frequency is measured using the arrival time of the maximum envelope value. However, because the true signal energy distribution is smoothed by the filter response, the center frequency of the filter does not represent the true frequency for the measured group time (Kodera et al., 1976; Rihaczek, 1968). To account for this effect, we calculate the frequency for the centroid of the energy distribution of the filtered signal, which has been called *energy reassignment* (Auger & Flandrin, 1995; Pedersen et al., 2003). Note that this new frequency is exactly equivalent to the instantaneous frequency found from the partial derivative of the phase at the group time (i.e., $\hat{\omega} = \frac{\partial \phi(t)}{\partial t}|_{t=t_{\max}}$; Auger & Flandrin, 1995; Kodera et al., 1976). Finally, we transform the measured group times to group velocities by dividing the interstation distance of the station pair under consideration by the group time. An example spectrogram is shown in Figure 3.

Due to the large volume of data, we automate the group velocity measurement procedure. Despite our quality control methods, outliers may remain present in the dispersion curves. However, an investigation into using data containing instrument calibrations and gaps has shown that the effects on dispersion curve measurements are minimal (see section S1 in the supporting information). Outliers are identified and removed during the surface wave tomography. Since our dispersion curve measurements lack uncertainties, we test several methods to assign relative uncertainties to group velocities measured from 1-year cross-correlation stacks in the supporting information (Holland & Welsch, 1977; Massy, 1965). We measure uncertainties by calculating dispersion curves for each station pair using randomized sets of 40-day cross-correlation stacks. We then use principal component regression to find a relationship between the interstation distance, period, inverse SNR, and the measured uncertainty. In general, we find that uncertainty increases with decreasing distance and increasing period (see section S2 in the supporting information).

3. Surface Wave Tomography

In the path-average approximation, each group velocity dispersion curve can be estimated to represent an average along the path between the corresponding station pair,

$$\overline{U(T)} = \frac{1}{\Delta} \int_P U(T, \theta, \phi) \mathrm{d}\Delta(\theta, \phi). \tag{2}$$

We construct a spherical shell of 32,071 grid nodes separated by 0.35° on average, which corresponds to a tessellation level of 9. The grid is centered on 33°N, 111°E and extends 30° in all directions. The grid node locations are derived through triangular tesselation of a sphere, as described by Z. Wang and Dahlen (1995) and first used in seismic tomography for Moho depth parameterization by van der Lee and Nolet (1997). The group velocities are parameterized on the grid via

$$U(T, \theta, \phi) = \sum_k w_k U_k(T, \theta_k, \phi_k), \tag{3}$$

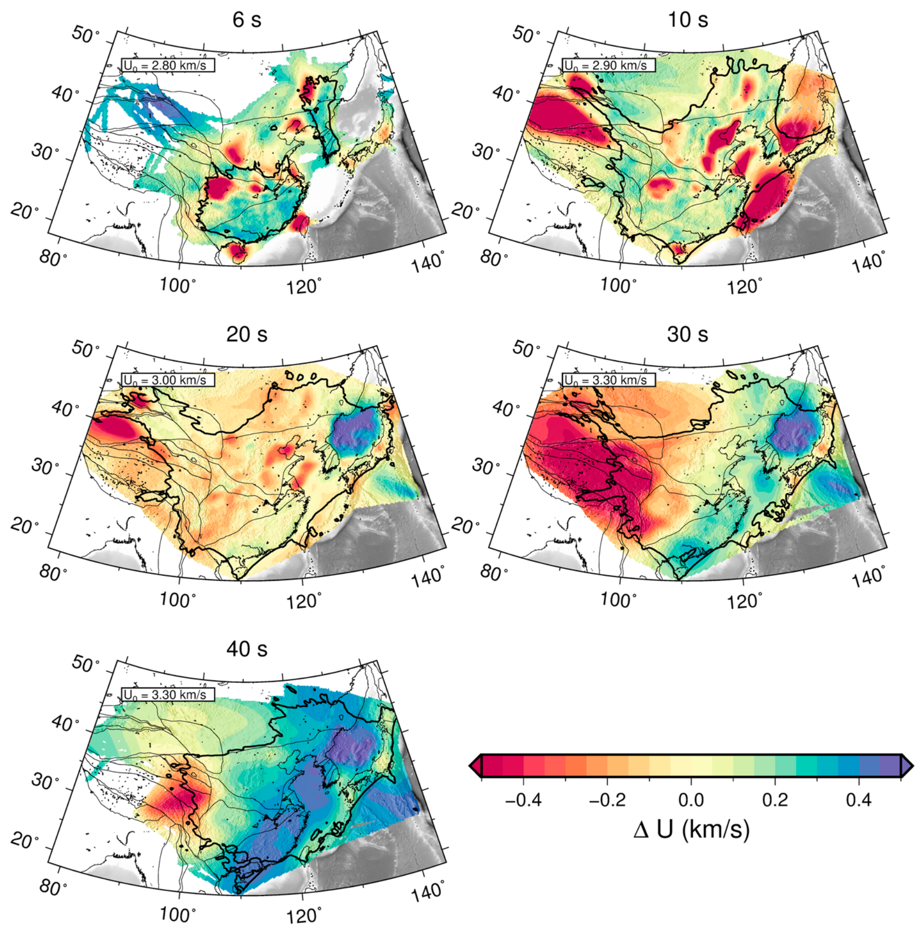

Figure 4. Rayleigh wave group velocities for periods 6, 10, 20, 30, and 40 s. Period labels are located at the top of each map. The color scale is shown on the bottom right and ranges within ±0.5 km/s. Each map's scale is relative to a center group velocity U_0, located at the top left of each map. The bold contours demarcate the regions used for the *S* velocity inversion and were determined using the normalized ray density maps (e.g., Figure S7 in the supporting information).

where *k* indexes the grid nodes. The dispersion curves are localized by inserting equation (3) into equation (2) for all measured paths and solving the resulting system of equations for $U_k(T, \theta_k, \phi_k)$. The inverse problem is solved using the LSMR routine of Fong and Saunders (2011). LSMR is an iterative conjugate gradient type method for solving least squares problems similar to the well-known LSQR method but has been shown to converge to an approximate solution sooner in certain situations (Fong & Saunders, 2011; Paige & Saunders, 1982). We construct a data vector **d** to be differences between our measured group velocities and the group velocities predicted by *ak135* (Kennett et al., 1995). The model vector **m** represents group velocity perturbations with respect to the *ak135* group velocity dispersion curve at every grid node. We minimize a misfit equation defined to be

$$S(\mathbf{m}) = (G\mathbf{m} - \mathbf{d})^T C_e^{-1} (G\mathbf{m} - \mathbf{d}) + \lambda_F^2 |F\mathbf{m}|^2 + \lambda_D^2 |I\mathbf{m}|^2, \tag{4}$$

where *G* is the raypath matrix relating the data vector **d** to the values at the model nodes of **m**, C_e^{-1} is the inverse of the data covariance matrix, *F* is a flattening matrix representing a discretized version of the first derivative operator, and *I* is the identity matrix. The λ factors are scalars representing the strength of the flattening and damping. The values for λ_D and λ_F are chosen by plotting tradeoff curves of model complexity versus fit to the data. The final group velocity maps are created by adding the *ak135* group velocity dispersion curve to **m**.

Before calculating **m**, we remove measurements with group velocities above 5 km/s, and if the period is below 30 s, we remove measurements with group velocities above 4.5 km/s. We conduct an initial inversion and calculate normalized residuals $r_i = \frac{d_i - \sum_j g_{ij} m_j}{\sigma_i}$, where σ_i is the estimated relative uncertainty for the *i*th datum. We

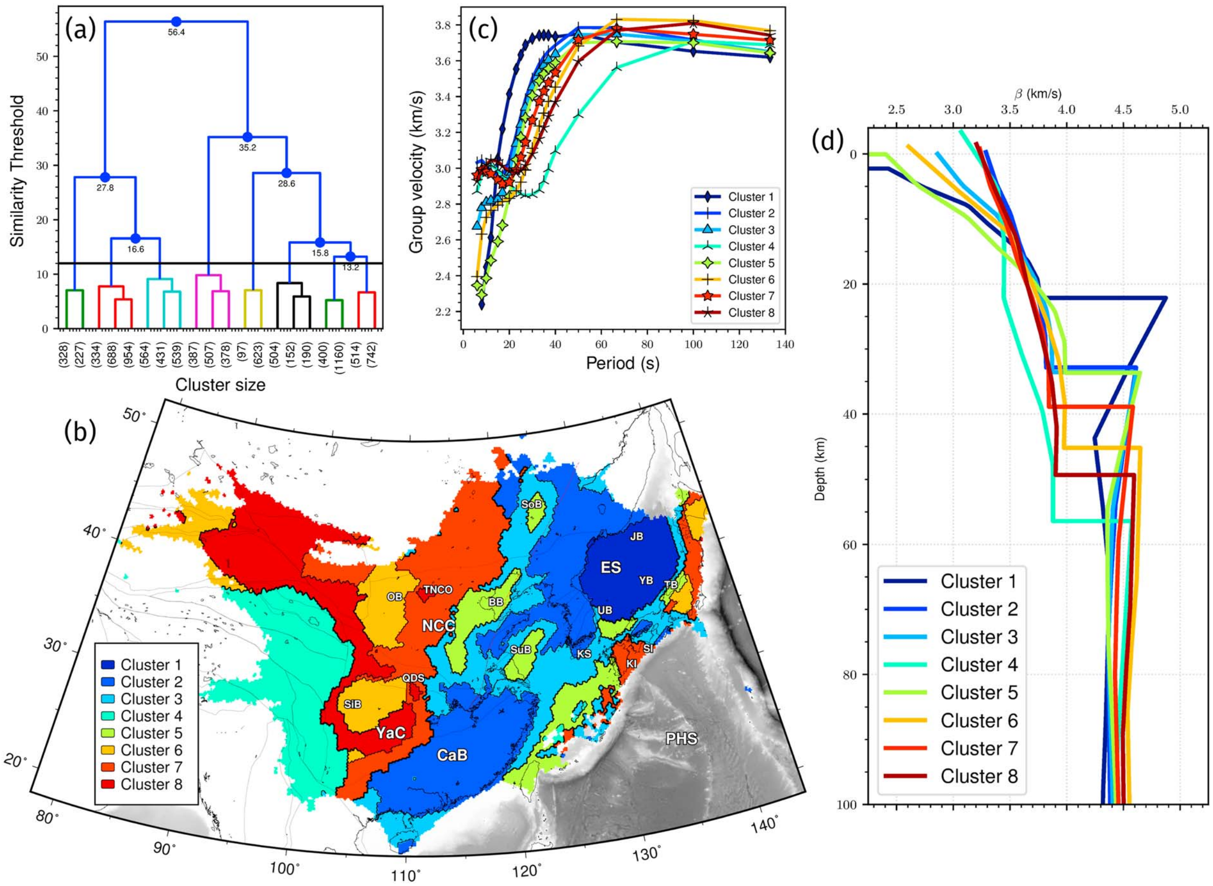

Figure 5. (a) Dendrogram showing agglomerated clusters. A horizontal line is drawn at a similarity threshold of 12. Below this line, similarly colored forks represent a single cluster. Above this line, numbers below nodes represent thresholds below which those clusters diverge. Numbers in parentheses on the *x* axis denote the number of dispersion curves in that cluster. (b) Map showing eight clusters under a maximum similarity threshold of 12.0. (c) Centroid dispersion curves. (d) Resulting *S* velocity models after inverting the centroid dispersion curves.

then identify and remove outliers in the normalized residuals by application of the median absolute deviation test (Miller, 1993). After outlier removal we perform another inversion to retrieve the final group velocity dispersion model.

To estimate the resolving power of the data, we (1) perform resolution testing by creating hypothetical Gaussian checkerboard models, (2) calculate a synthetic data vector by multiplying the hypothetical model by *G*, and (3) add Gaussian noise at the same SNR as the data. Resolution test results (section S3 in the supporting information) show that our data best allow us to resolve anomalies between roughly 96° and 138°E and between 18° and 48°N. Anomalies to the far west are typically ill-retrieved below a size of 4° for all periods. We achieve 0.5° resolution in East Asia at periods $\leq$ 30 s and achieve 1° resolution at periods $\leq$ 60 s. Anomalies smaller than 1° in the Yellow Sea are typically smeared in the SW-NE direction. Anomalies in the East Sea smaller than 4° are smeared in the SE-NW direction, following the dominant raypath direction.

Maps for periods 6, 10, 20, 30, and 40 s are shown in Figure 4. The contours mark the boundaries of regions used in the inversion for shear wave velocity structure. These boundaries are determined using the normalized ray density maps for each period (Figure S7 in the supporting information). At 6-s period, we use data where the ray density is above 20%, and above 6-s period we use a 5% threshold. At short periods (< 15 s), we observe all major sediment basins in the region, except for the Bohai basin at 6-s period. Starting at 15-s period, we begin to see high velocities in the East Sea, due to the thinner oceanic type crust in that region. As the period increases, we begin to see variations in the group velocities due to lateral heterogeneities in Moho depth as well as upper mantle velocities. Around 30-s period we observe the well-known east-west dichotomy in East Asia, due to thinned lithosphere in the east gradually thickening moving west.

10.1029/2018JB016060

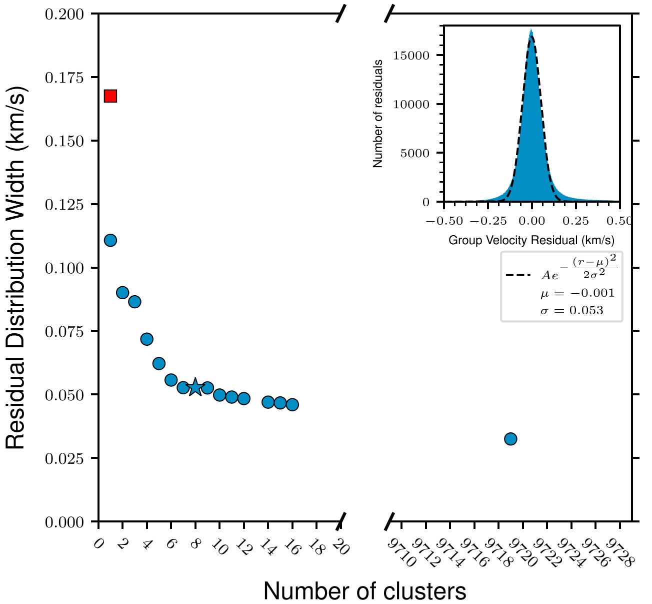

Figure 6. Residual distribution widths calculated for path averages using dispersion models with different amounts of clusters. The red square shows the result from using our single-layer crust *ak135* model. (Inset) Residual distribution with Gaussian function fit for the (star) eight-cluster model.

4. Cluster Analysis

4.1. Heirarchical Agglomerative Clustering

We perform a cluster analysis of the localized dispersion curves via an agglomerative clustering method. We combine our ambient noise data set with localized group velocity data in the period range 50–133 s from the global dispersion model of Ma et al. (2014), which was used in the development of the LITHO1.0 model (Pasyanos et al., 2014). The similarity between two dispersion curves is defined as $s_{ij} = \sqrt{\sum_k (U_i(T_k) - U_j(T_k))^2}$. All localized dispersion curves begin as their own cluster and at each step clusters are merged using Ward's method (Ward, 1963), which seeks to minimize loss of information when clustering data by minimizing the total variance within a cluster after merging. When building the similarity matrix s_{ij}, we compare the normalized ray density at each grid node for every period. For 6-s period data, we check if both dispersion curves have a normalized ray density value greater than 0.20, and for periods greater than 6-s period, we check if the normalized ray densities are greater than 0.05. If, for example, one dispersion curve has reliable 6-s period data while the other does not, the 6-s period data are not used in calculating the similarity between the two localized dispersion curves. We constructed a dendrogram, shown in Figure 5a, to help guide our choices of maximum cluster similarity thresholds used for determining the number of clusters. From Figure 5a, we can immediately see two distinct clusters that have a large distance between them, and these two clusters represent the east-west dichotomy in East Asia. Below a threshold of 35, Tibet appears as a third cluster, and the fourth cluster to appear are basins in the east. The fifth cluster to appear is the East Sea. Next, the basins in the west appear as a separate cluster, possibly distinct from the basins in the east due to their cratonic upper mantle nature. The Korean peninsula and the SCB appear as a single cluster, lending support for their tectonic affinity. We also see that northern Japan has dispersion characteristics more similar to western Asia, while southern Japan is more similar to the eastern portion. An example map showing a set of eight clusters using a similarity threshold of 12 is shown in Figure 5b. The number of clusters quickly rises with decreasing threshold value, where each new cluster represents a gradation between two prior clusters. However, the fit to the data improves progressively less with increasing cluster amounts.

4.2. Cluster Data Fit

We create a set of clustered dispersion models by varying the maximum similarity threshold and assigning each node in a cluster to its centroid dispersion curve. We then calculated path averages for all raypaths in our data set to compare our path data to the dispersion curves predicted by each cluster model. We calculated residuals for each path and then estimated the width of the residual distributions from the standard deviation of best fitting Gaussian functions (Figure 6). We also calculate residuals for the initial model where each node is its own cluster, essentially representing the full 2-D surface wave tomography result. For our *S* velocity inversions, we use *ak135* with a single-layer crust as an initial model. Compared to that model, our one-cluster dispersion model, representing the average dispersion curve for the region, reduces the variance in group velocity predictions by 60%. We observe 42% variance reduction going from one to six clusters, 8% variance reduction going from 6 to 16 clusters, and 11% variance reduction when the number of clusters increases from 16 to 9,719. Given the spatial distribution of our group velocity measurements, only a relatively small set of centroid dispersion curves are necessary to explain the data to a satisfactory level. Amazingly, without any formal prior knowledge of the region, the cluster analysis naturally yielded distinct clusters that strongly resemble large-scale tectonic provinces. In the following section, we discuss our methodology for inverting group velocity dispersion curves, and then we perform several inversions. We first invert the centroid dispersion curves shown in Figure 5c and show that by using the resulting *S* velocity models as reference models for the full 3-D inversion, we can improve the predictive power of the final model.

5. Three-Dimensional *S* Velocity Inversion

5.1. Inversion Methodology

The inversion for *S* velocity variations is done according to

$$\delta U(T) = \int_0^a \left(K_\beta(T,r)\delta\beta + K_\alpha(T,r)\delta\alpha + K_\rho(T,r)\delta\rho\right) \mathrm{d}r + \sum^{N_d} \left[K_d(T)\right]_-^+ \delta d, \tag{5}$$

where K_β, K_α, K_ρ, and K_d are the so-called group velocity sensitivity kernels for small variations in *S* wave velocity $\delta\beta$, *P* wave velocity $\delta\alpha$, density $\delta\rho$, and boundary layer radius δd with respect to a reference 1-D model, respectively, and δU is the difference between the observed and predicted dispersion. We couple variations in *P* wave velocity and density to *S* wave velocity by setting $\frac{\partial ln\alpha}{\partial ln\beta} = 0.58$ and $\frac{\partial ln\rho}{\partial ln\beta} = 0.25$ in both the crust and mantle (Schmid et al., 2006, 2008; Shapiro & Ritzwoller, 2002). Attempts to use the relations of Brocher (2005) for the crust did not significantly change the results. We estimate the group velocity sensitivity kernels by first calculating the phase velocity sensitivity kernels and then applying Rodi et al. (1975) to numerically calculate the group velocity sensitivity kernels. K_d is calculated according to equation (9.35) in Dahlen and Tromp (1998) for the Moho discontinuity. Using the coupling relations, we can define the kernel $K = K_\beta + K_\alpha \frac{\partial\alpha}{\partial\beta} + K_\rho \frac{\partial\rho}{\partial\beta}$ and simplify equation (5) to

$$\delta U(T) = \int_0^a K(T,r)\delta\beta \mathrm{d}r + K_{\mathrm{Moho}}(T)\delta M. \tag{6}$$

Next, we expand $\delta\beta(r)$ onto a set of basis functions $h_i(r)$,

$$\delta\beta(r) = \sum_i \gamma_i h_i(r). \tag{7}$$

To be consistent with the lateral linear interpolation on the model grid, we use linear functions $h_i(r)$ defined at knot locations r_i. We use two sets of linear splines for the crust and the upper mantle. We use eight evenly spaced splines in the crust from the surface to the Moho with a spacing of 5 km if the Moho is at 35 km depth. We use 19 evenly spaced splines in the mantle from the Moho to 395 km depth with a spacing of roughly 20 km and a final knot at 410 km depth. For the Moho depth perturbation we set $\delta M = \gamma_M$. We insert the basis function expansion of $\delta\beta(r)$ and δM into equation(6) to get

$$\delta U(T) = \sum_i \gamma_i \int_0^a K(T,r)h_i(r)\mathrm{d}r + K_{\mathrm{Moho}}(T)\gamma_M. \tag{8}$$

In practice, a dispersion curve is measured on a set of periods $T_i = T_1, T_2, \dots, T_n$, allowing us to create a linear system of equations

$$\begin{pmatrix} \delta U(T_1) \\ \delta U(T_2) \\ \vdots \\ \delta U(T_n) \end{pmatrix} = \begin{pmatrix} \int K(T_1,r)h_1(r)\mathrm{d}r & \int K(T_1,r)h_2(r)\mathrm{d}r & \dots & K_d(T_1) \\ \int K(T_2,r)h_1(r)\mathrm{d}r & \int K(T_2,r)h_2(r)\mathrm{d}r & \dots & K_d(T_2) \\ \vdots & \vdots & \ddots & \vdots \\ \int K(T_n,r)h_1(r)\mathrm{d}r & \int K(T_n,r)h_2(r)\mathrm{d}r & \dots & K_d(T_n) \end{pmatrix} \begin{pmatrix} \gamma_1 \\ \gamma_2 \\ \vdots \\ \gamma_M \end{pmatrix},$$

which can be condensed into the matrix equation $\mathbf{d}_U = \mathcal{K}_U\boldsymbol{\gamma}$. We construct a similar system of equations for phase velocities using the phase velocity sensitivity kernels, which we write as $\mathbf{d}_c = \mathcal{K}_c\boldsymbol{\gamma}$.

We define the objective function

$$S(\boldsymbol{\gamma}) = |\boldsymbol{d}_U - \mathcal{K}_U\boldsymbol{\gamma}|^2 + |\boldsymbol{d}_c - \mathcal{K}_c\boldsymbol{\gamma}|^2 + \lambda_F^2|F\boldsymbol{\gamma}|^2 + \lambda_D^2|I\boldsymbol{\gamma}|^2, \tag{9}$$

where F is a first-order finite difference operator, I is the identity matrix, and the factors λ_F and λ_D control the strength of the regularization. Minimizing this objective function with respect to the basis function coefficients $\boldsymbol{\gamma}$ leads to the system of equations

$$\begin{pmatrix} \mathcal{K}_U \\ \mathcal{K}_c \\ \lambda_F F \\ \lambda_D I \end{pmatrix} \boldsymbol{\gamma} = \begin{pmatrix} \boldsymbol{d}_U \\ \boldsymbol{d}_c \\ \mathbf{0} \\ \mathbf{0} \end{pmatrix}. \tag{10}$$

We construct an a priori model covariance matrix C_m by sampling the LITHO1.0 model at our model nodes at each depth knot for a rough estimate of the level of variation in the material properties and further modify the matrix equation we are solving to be

$$\begin{pmatrix} \mathcal{K}_U C_m^{\frac{1}{2}} \\ \mathcal{K}_c C_m^{\frac{1}{2}} \\ \lambda_F F \\ \lambda_D I \end{pmatrix} C_m^{-\frac{1}{2}} \boldsymbol{\gamma} = \begin{pmatrix} \boldsymbol{d}_U \\ \boldsymbol{d}_c \\ \mathbf{0} \\ \mathbf{0} \end{pmatrix}, \tag{11}$$

which we condense as $A\boldsymbol{\gamma}' = \boldsymbol{d}$. We solve this system of equations using singular value decomposition and retrieve the final model via $\boldsymbol{\gamma} = C_m^{\frac{1}{2}}\boldsymbol{\gamma}'$. To create the final 3-D model, this is repeated at every node in the model grid which has reliable ambient noise dispersion data as determined from the normalized ray densities (e.g., Figure S7 in the supporting information and Figure 4).

5.2. Cluster Centroid *S* Velocity Models

We first focus on the eight-cluster dispersion model because it highlights many of the large-scale tectonic features in the region. We inverted the eight centroid dispersion curves in Figure 5c, and the results are shown in Figure 5d. To create each 1-D cluster reference model, we set the initial mantle model within each cluster to be *ak135*, with a single layer crust formed from an average of the *ak135* crustal layers. Using an initial 3-D Moho model incorporating information from previous receiver function studies (S.-J. Chang & Baag, 2007; Y. Li et al., 2014; Pasyanos et al., 2014; Ramesh et al., 2005), the Moho depths are set corresponding to the average within the cluster (see section S4 in the supporting information for details). We did not allow the Moho depth to vary during the inversion for the 1-D cluster reference models.

Cluster 1 corresponds to the East Sea, which has a thin crust and a thin, high-velocity lithosphere. When the number of clusters is increased, the East Sea breaks into two separate clusters, an inner region and an eastern flank. The inner region has a shallower Moho, while the eastern flank has much lower crustal velocities near the surface, indicative of sediments. The base of the crust and the uppermost mantle have higher velocities in the eastern flank than in the inner region. The eastern flank also has lower velocities at the base of the lithosphere, while the inner region has lower velocities at greater depths.

Cluster 5 corresponds to the various basins in the area. Along the edge of cluster 1, we observe two back-arc rift structures, the Ulleung basin to the south and the Toyama basin to the east (Chough & Barg, 1987; Ishiyama et al., 2017; Kim & Yoon, 2017). To the west of the Ulleung and Toyama basins, we observe the Songliao, Bohai Bay, and Subei Yellow Sea basins, which were formed in several rifting episodes during the Mesozoic and Cenozoic eras (Hu et al., 2001; Menzies et al., 1993, 2007; Tian et al., 1992; Ye et al., 1985). This cluster shares similar Moho depths and mantle structures with clusters 2 and 3, so that clusters 2, 3, and 5 mainly differ by their crustal structure.

Cluster 4 represents Tibet, with the deepest Moho. We observe low velocities in the crust at around 25 km depth, corroborating other geophysical studies reporting low-velocity layers in Tibet (H. Li et al., 2009; Yang et al., 2012; Yao et al., 2008). Cluster 6 matches well with the Yangtze craton in the SCB, and the Ordos block, and it has the highest upper mantle velocities. Cluster 6 has similar upper mantle features with clusters 4 and

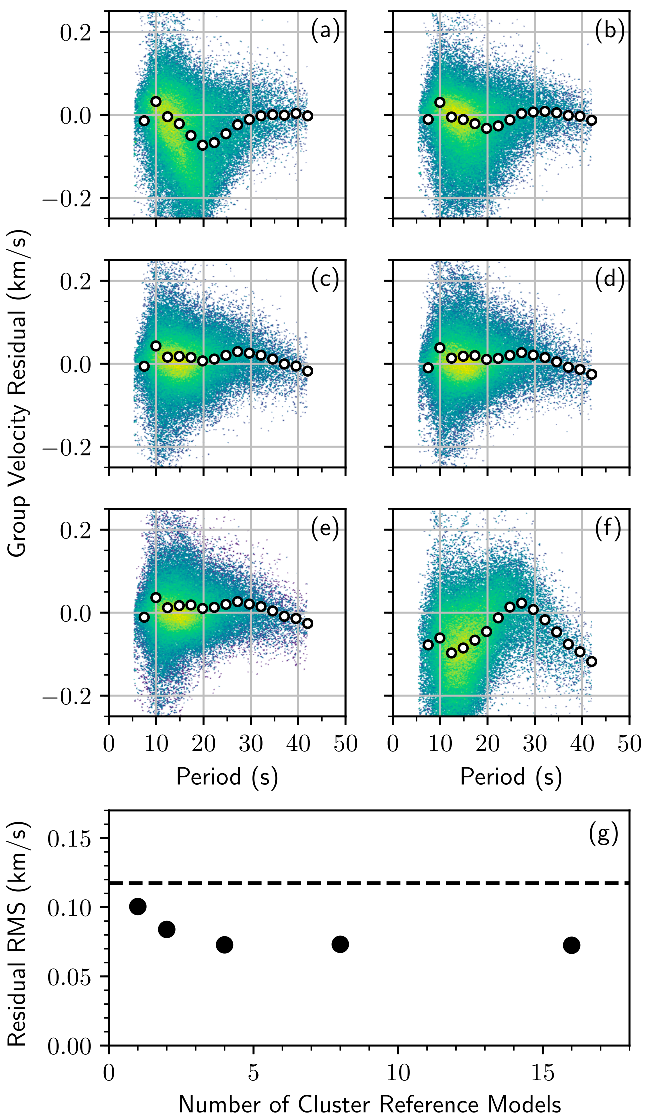

Figure 7. Two-dimensional histograms of residuals for *S* velocity models resulting from using reference models: (a) one-cluster reference model, (b) two-cluster reference model, (c) four-cluster reference model, (d) eight-cluster reference model, and (e) 16-cluster reference model. (f) Residuals for the LITHO1.0 model. White circles show mean values in 15 period bins, while their uncertainties are too small to be seen. Colors are on a log scale, and bright yellow colors indicate a high density of points. (g) Residual RMS as a function of the number of cluster reference models. The dashed black line is the LITHO1.0 residual RMS. RMS = root-mean-square.

8. Clusters 7 and 8 share similar crustal structure, but upper mantle velocities in cluster 7 appear to be lower than those in clusters 4, 6, and 8.

Clusters 6 and 7 also appear in northern Japan, while southern Japan is mostly characterized by clusters 2 and 3. However, the region around Kyushu Island appears to be characterized by cluster 7. The appearance of different clusters around Japan may be attributed to whether or not there are sediments in the crust, as well as to variations in the upper mantle due to differences in the subducting slabs. The area in cluster 6 in northern Japan is characterized by a deeper Moho relative to the rest of Japan and is overlain with Neogene and Quaternary sediments (Van Horne et al., 2017; D. Zhao & Hasegawa, 1993). The depth to the subducting Pacific slab also begins to dip from 100 to 200 km, whereas in the cluster 7 region the depth to the slab stays roughly constant at 100-km depth along the middle (D. Zhao et al., 1994, 1997). In southern Japan, the correspondence with clusters 2 and 3 is due to the younger Phillipine Sea slab subducting at a shallower angle compared to the much older Pacific slab. The Phillipine Sea slab is found at a depth of 30 km underneath Shikoku and 60 km under the main island, to roughly 150 km depth at the northern coast (Asamori & Zhao, 2015; Nakajima et al., 2009). Underneath Kyushu, the Phillipine Sea Slab dips steeply from 20 km depth in the east, 120–150 km in the center, and 300–350 km depth under the western coast (Asamori & Zhao, 2015).

5.3. Three-Dimensional *S* Velocity Model

We constructed 3-D *S* velocity models by inverting local dispersion curves at each node in the model grid. We use ambient noise data in the period range 6–40 s and earthquake data in the range 50–133 s. We also jointly invert earthquake phase velocity data in the period range 28.57–200 s. The localized earthquake group and phase velocity dispersion curves are constructed using the global dispersion model of Ma et al. (2014). After constructing each 3-D model, we forward calculate Rayleigh wave group velocity curves predicted by the models and compare them against the measured dispersion curves. We randomly sample our dispersion curve data set to select 9,872 interstation paths. For each path, we calculate an average 1-D model along the path and then predict a group velocity dispersion curve. We calculate a residual, $r = U^{obs.} - U^{pred.}$, for each data point. At the same time, we calculate an average model along the path using the LITHO1.0 model (Pasyanos et al., 2014) and perform the same measurements. The LITHO1.0 model is distributed as a set of 1-D models on a global tessellated grid similar to our own, thus allowing us to consistently calculate path average models. To construct the path-averaged LITHO1.0 models, we follow the LITHO1.0 model depth parameterization (i.e., Table 1 of Pasyanos et al., 2014) and find the path-averaged thickness and material properties of each layer. An example path-averaged model is shown in Figure 11.

We tested the effects of using different reference velocity models, as opposed to using *ak135* for the entire region. We construct a priori 3-D *S* velocity models by assigning the 1-D cluster *S* velocity models (e.g., Figure 5d) to the appropriate nodes in the model grid. The velocity structure is initially identical within a cluster, but the Moho depth varies according to our 3-D Moho depth model (Figure S8 in the supporting information). A comparison of the residuals is shown in Figure 7, and the LITHO1.0 residuals are shown in Figure 7f. Using the one-cluster reference model leads to high *S* velocities in the lower crust for the eastern portion of the model, thus overpredicting group velocities in the period range 5–30 s. As the first two clusters to form are the east and west, this is evidence that the two halves of the region are truly different in structure. As the number of cluster reference models increases, the resulting *S* velocity models become less biased, but the rate of improvement decreases, as in Figure 6. Visual comparisons of the 3-D *S* velocity inversion results using different reference models are shown in Figures S10 and S11 in the supporting information. While improve-

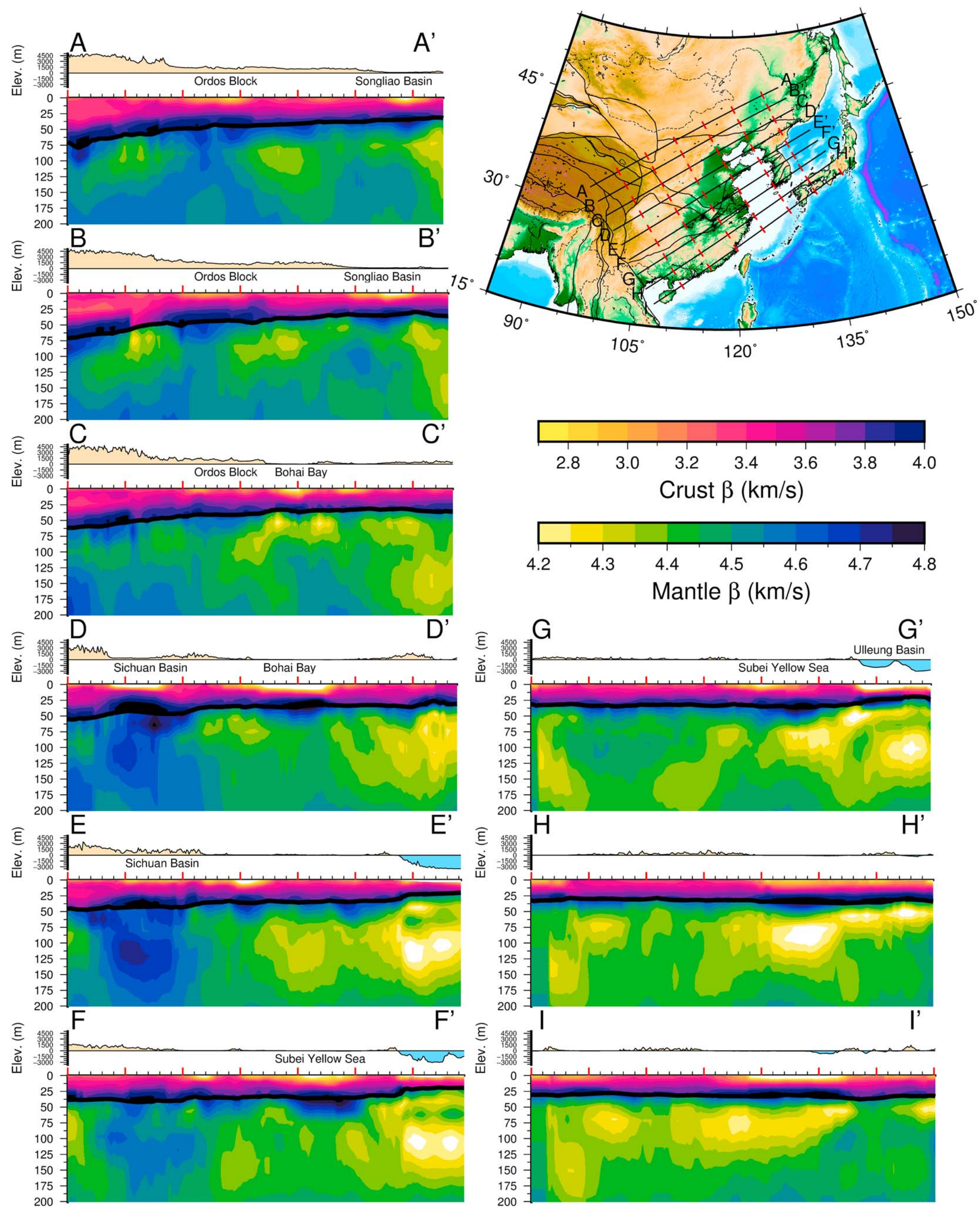

Figure 8. Transects trending from the SW to the NE. The transects are scaled such that their lengths are comparable. The red major tick marks on the *x* axis represent 500-km increments and correspond to the red tick marks on the map in the upper right. Topography and locations of major surface basins are shown above each transect.

ments to the overall data fit are slight when the number of clusters increases from 4 to 16, the 16-cluster reference model results in a smoother *S* velocity inversion result. We therefore prefer the 16-cluster model for 3-D structural interpretation. Vertical transects through the model are shown in Figures 8 and 9. We also show horizontal depth sections through the model in Figure 10.

In the shallow crust, we observe low velocities in the major basins in the region. The lowest velocities are found in the Bohai Bay, Ulleung, Yamato, and Japan basins. Low velocities in the Subei Yellow Sea, Sichuan, and Songliao basins have similar values, while the Ordos appears to have the highest of the low velocities. Outside of the major basins, velocities in the upper crust are fairly homogenous. However, in the lower crust from 20 to 40 km depth we find high velocities under the Sichuan basin. High velocities appear in the East Sea

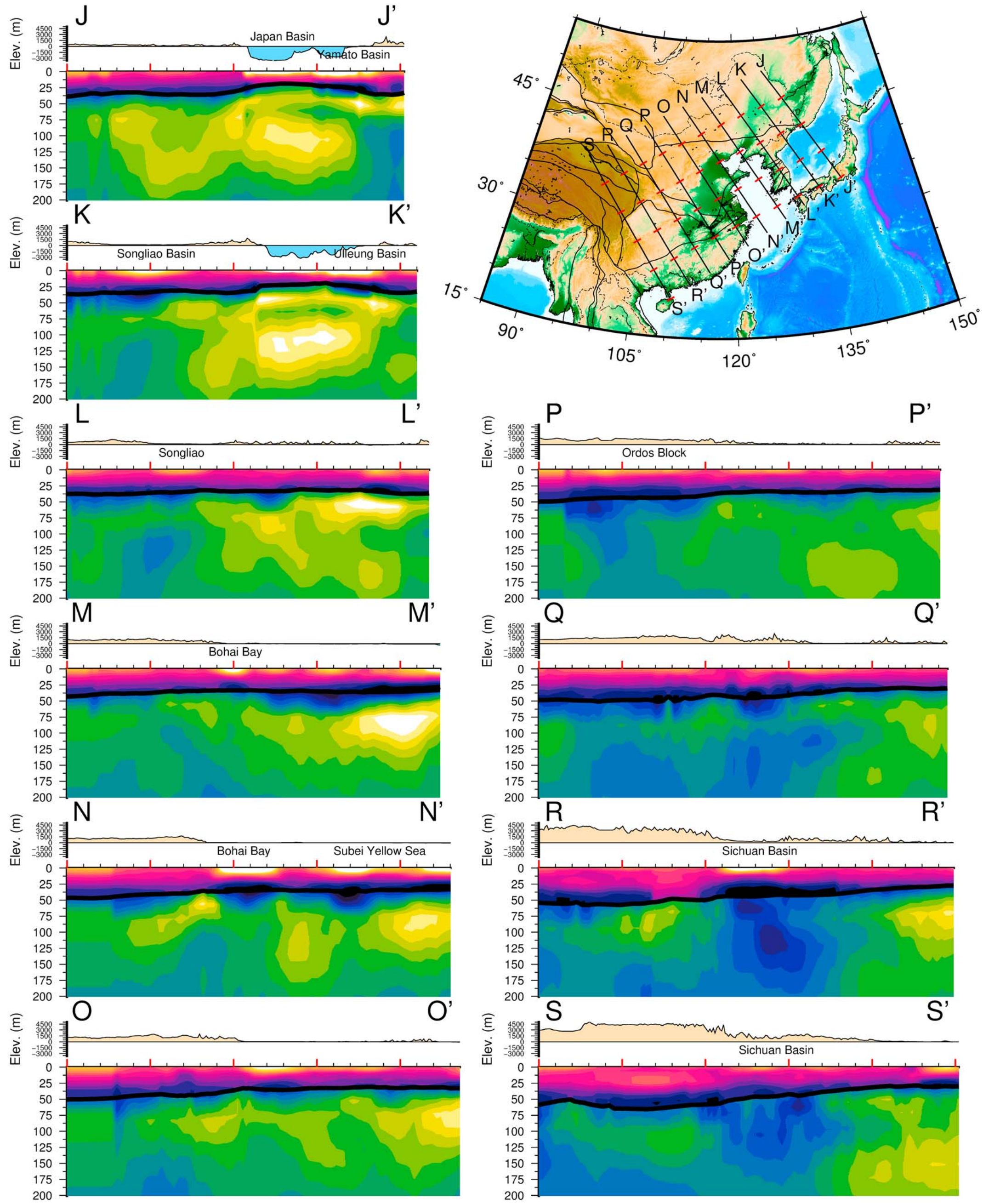

Figure 9. Transects trending from the NE to the SW. Colors for the crust and mantle are on the same scale as in Figure 8. The red major tick marks on the *x* axis here also represent 500-km increments.

around 20 km depth due to the thin crust in that region. Velocities in Tibet begin high near the surface but appear to drop around 20-km depth before increasing again. This low-velocity zone in Tibet, also in transects A-A′, B-B′, R-R′, and S-S′, has been shown in previous studies and is thought to be due to the presence of partial melt or aligned anisotropic minerals (Jiang et al., 2014; Kind et al., 1996; Liang & Song, 2006; Nelson et al., 1996; Wei, 2001; Yang et al., 2012).

The Yangtze craton shows up as a prominent high-velocity region in transects D-D′, E-E′, R-R′, and S-S′, and persists down to 200-km depth. The Ordos block can be seen in transects A-A′, B-B′, C-C′, Q-Q′, and P-P′; however, the velocities are not as high as in the Yangtze craton, and their depth is shallower. Similar high velocities in the mantle are found underneath the Songliao basin. As we move from transect A-A′ to I-I′, we see an increase in low-velocity regions in the upper mantle, with the lowest velocities found beneath the East

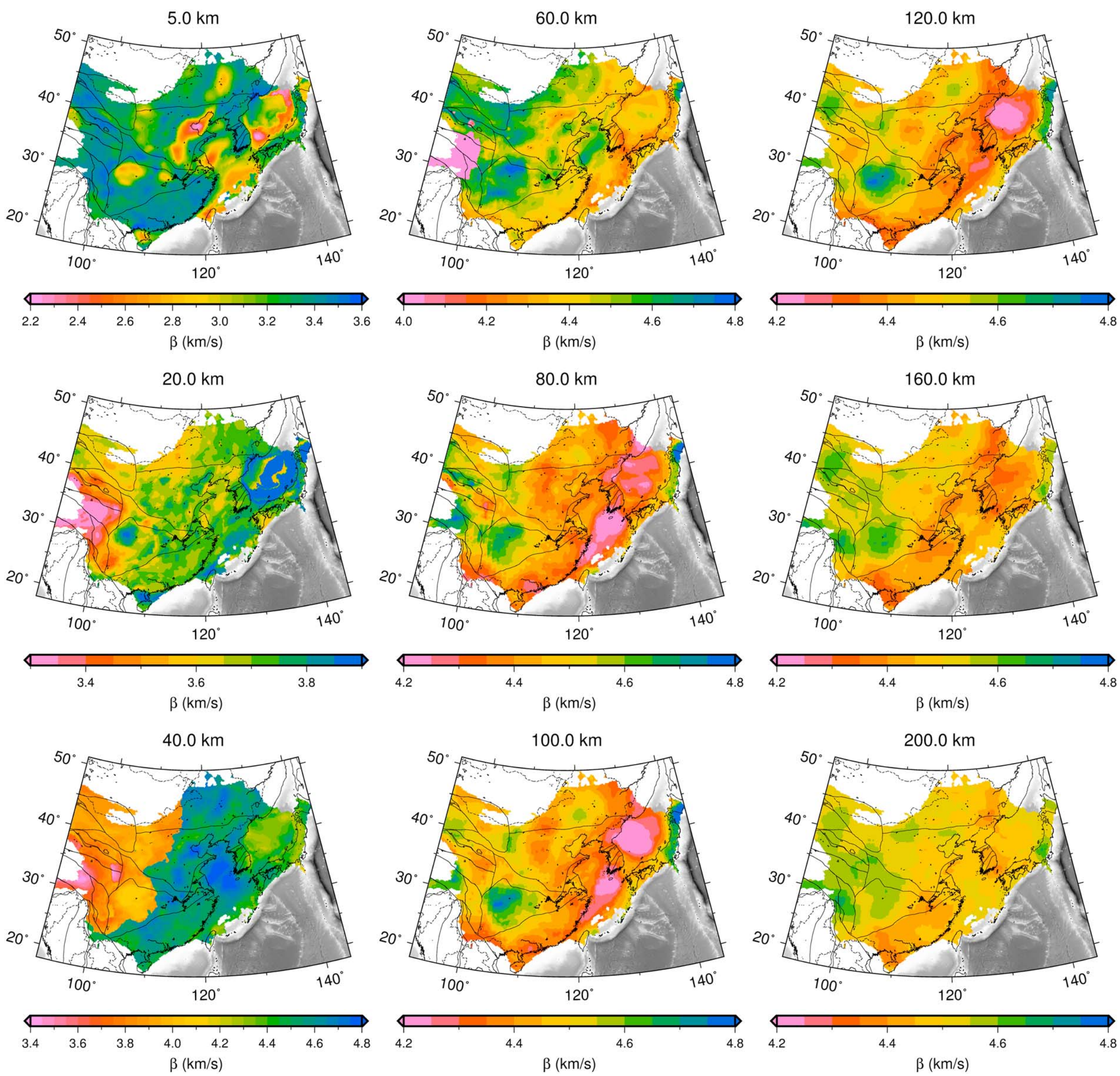

Figure 10. Horizontal depth slices through our model. Depths are found above each panel.

Sea. We see this in transects J-J′ through S-S′, which go from the northeast to the southwest, and this trend can also be observed in the horizontal depth maps at 60–200 km depth. This has been identified in previous studies as due to lithospheric thinning. Geochemical evidence from kimberlites indicate a thick (> 180 km) and cold lithosphere under the NCC prior to the Paleozoic, but basalt-borne xenoliths give evidence for thin (< 80 km) and hot lithosphere in the Cenozoic (e.g., Gao et al., 2002; Menzies et al., 1993, 2007; F.-Y. Wu et al., 2003; Y.-G. Xu, 2001). Velocities in the mantle decrease moving from the Yangtze craton to the Cathaysia block, where previous geophysical and geochemical studies in the region found evidence for active rift settings and lithospheric thinning in the Mesozoic (e.g., Lebedev & Nolet, 2003; C. Li & van der Hilst, 2010; Y. Wang et al., 2008; F. Wu et al., 2005). Clusters 1, 2, 3, and 5 in Figure 5b therefore represent a broad zone of lithospheric deformation.

Below the East Sea we observe a two-tiered low-velocity structure in the upper mantle, visible in transects E-E′, F-F′, J-J′, and K-K′. On the flanks of this feature we observe high-velocity regions immediately below the Moho, which was also observed in *Pn* traveltime study of Hong and Kang (2009) and was interpreted as underplated high-velocity material (White & McKenzie, 1989). This might also explain the appearance of high velocities in the uppermost mantle underneath the rift basins in the east. However, at 60 km depth we begin to see a ring

Table 1
Comparison of the RMS Model Differences Between This Study, W. Shen et al. (2016), LITHO1.0, and the Uncertainties Reported by W. Shen et al. (2016)

Depth (km)	$\sqrt{\frac{1}{M}\sum r^2_{\mathrm{Shen}}}$ (km/s)	$\sqrt{\frac{1}{M}\sum r^2_{\mathrm{LITHO}}}$ (km/s)	$\sqrt{\frac{1}{M}\sum \sigma^2_{\mathrm{Shen}}}$ (km/s)
20	0.079	0.160	0.044
40	0.226	0.315	0.108
60	0.140	0.190	0.135
80	0.112	0.114	0.125
120	0.101	0.107	0.155

Note. Here we define r to be the model difference $r = m_{\mathrm{Shen,LITHO1.0}} - m_{\mathrm{this\ study}}$. RMS = root-mean-square.

of low velocities around the edges of the East Sea, and these low velocities extend southward through the Strait of Korea to the Okinawa Trough. At 80–100 km depth, these low velocities begin to broaden laterally and cover large areas. The low-velocity anomaly persists below Jeju Island down to 120 km depth and down to 140–160 km depth under the East Sea.

At 80–100 km depth, we see high velocities in northern Japan, which is roughly the depth to the top of the subducting Pacific plate. As the depth to the plate increases to the west, we also observe persistent high-velocity anomalies down to 200 km going westward. In southwestern Japan, a high-velocity anomaly under Shikoku Island is observed at 40–60 km depth, perhaps due to the subducting Phillipine Sea plate. However, between 100 and 180 km depth, the slab is only observed slightly to the northeast as well as underneath Kyushu, but not in between. This has been interpreted in other studies as a slab window, which may be caused by segmentation due to subduction of mechanically weak lithosphere (Asamori & Zhao, 2015; Huang et al., 2013; D. Zhao, 2017; D. Zhao et al., 2012). This would be consistent with our cluster analysis results, which show a change from clusters 6 and 7 in the north, to clusters 2 and 3 in the southwest, to cluster 7 around Kyushu Island.

We compare our model to LITHO1.0 and to the work of W. Shen et al. (2016), who used data from over 2,000 seismic stations across East Asia to produce a high-resolution 3-D isotropic *S* wave velocity model. Comparisons between our model, LITHO1.0, and W. Shen et al. (2016) are shown in Figure S12 in the supporting information. We compute RMS model differences, and we compare them with the RMS uncertainty calculated from the reported uncertainties in the model of W. Shen et al. (2016; Table 1). We find that our models have the greatest differences in the crust and uppermost mantle, while below 60 km depth the differences between our models are comparable to the uncertainties reported by W. Shen et al. (2016). At 20 km depth, our model has similar velocity patterns with W. Shen et al. (2016), but we show higher velocities in the SCB, northeast China, and Japan. LITHO1.0 shows higher velocities overall, with a low-velocity region in the Cathaysia block. Our models show the greatest differences at 40 km depth, which is most likely due to differences in crustal thickness. Taking into account teleseismic receiver function study results (S.-J. Chang & Baag, 2007; Y. Li et al., 2014; Ramesh et al., 2005) moves the 40-km Moho boundary contour west relative to that shown in W. Shen et al. (2016) and in LITHO1.0. At 60 km depth, our model depicts higher velocities in the Yangtze and Ordos cratons compared to W. Shen et al. (2016), while LITHO1.0 shows a broad region of high velocities in the west. We do not observe what W. Shen et al. (2016) call a *horseshoe* shaped anomaly at 80 km depth and instead see a broad region of low velocities underneath the eastern portion of the NCC. This could be due to our Rayleigh wave group velocity dispersion models being smoother than those derived by W. Shen et al. (2016), who seem to show more short-wavelength features. However, our deeper structures are constrained by Rayleigh group and phase dispersion information from periods as long as 200 s (Ma et al., 2014), while the longest periods used in W. Shen et al. (2016) are 70 s. Our model also shows high velocities at 80 and 120 km depth underneath Japan, which is due to the subducting Pacific slab. These high velocities appear to be shifted to the east in LITHO1.0, and only appear weakly at 120 km in W. Shen et al. (2016).

We also find that our models predict Rayleigh wave group velocity measurements derived from earthquakes in the region. We searched the data set of Ma and Masters (2014) to find earthquake-station paths that are within our model region, and for each of these paths, we followed the same procedure of group velocity curve prediction as before. An example path is shown in Figure 11. The measurements were made for a magnitude

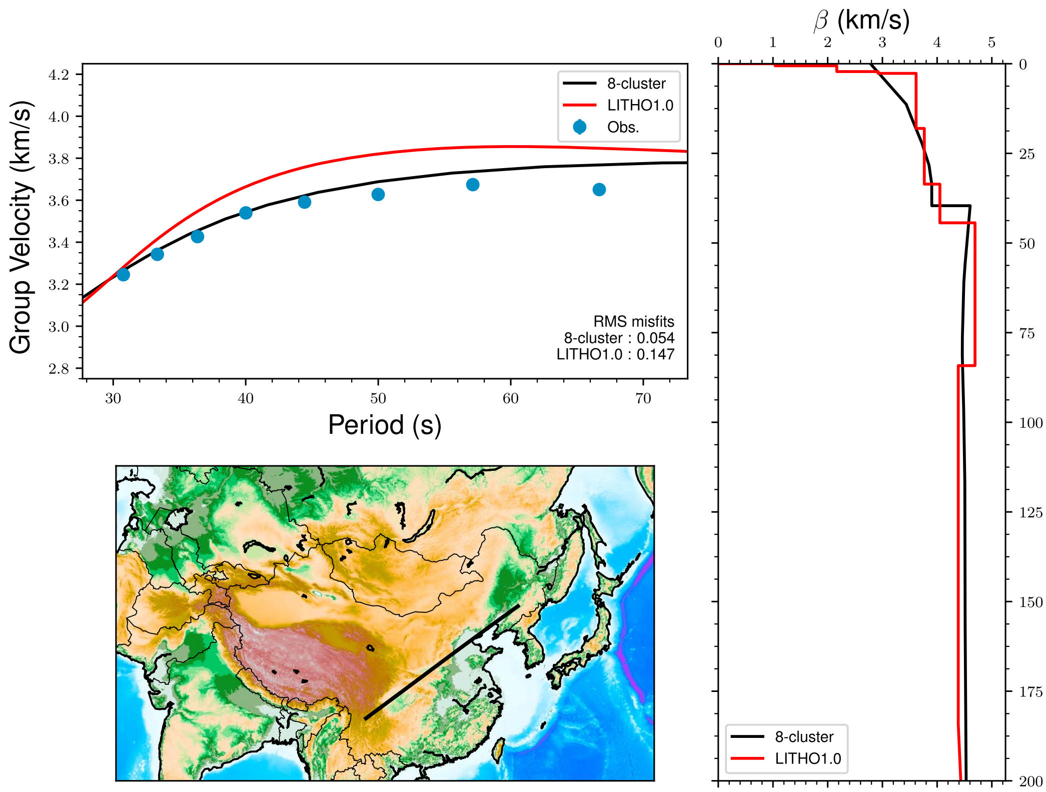

Figure 11. (top left) Plot showing earthquake group velocity measurements compared with the model predictions. Root-mean-square misfits are in units of kilometers per second. (bottom left) Map showing the great circle path from event to station. (right) Average *S* velocity models along the path for our eight-cluster inversion result and the LITHO1.0 model. The group velocity dispersion curves depicted in the top left are calculated from these path-averaged models. Note the shallower Moho depth and negative velocity gradient below the Moho for our model.

M_w 5.6 earthquake that occurred in western Sichuan on 19 November 1998 at 11:38 UTC. Our model is able to achieve a variance reduction of 87% with respect to the LITHO1.0 model for this path. Histograms of the earthquake group velocity misfits for the paths found in the model region are shown in Figure 12. In general, we find that the LITHO1.0 model tends to overpredict group velocities in the period range 30–70 s for this region. This could be partly due to the LITHO1.0 model's deep Moho in East Asia and partly due to parameterization of the uppermost mantle. The use of a constant high-velocity lithosphere might not be appropriate for the eastern portion of the study region, which has undergone significant lithospheric thinning.

6. Conclusions

We have collected continuous vertical-component data from over 1,000 stations in East Asia and measured fundamental mode Rayleigh wave group velocity dispersion by cross-correlating processed ambient seismic noise records. We then used these measurements to create maps of localized group velocities for the period range 6–40 s, and we combined our ambient noise results with the earthquake-based global dispersion model of Ma et al. (2014). We performed a cluster analysis of the localized group velocity maps and found that a set of as few as eight clusters is sufficient to predict the data. We inverted the centroid dispersion curves for a set of *S* velocity models that explain the general features found in each cluster.

Next, we performed 1-D inversions for *S* velocity perturbations at each of our grid nodes well covered by the data. We show that using the centroid *S* velocity models as reference models improves the results of the inversion compared to using *ak135* as a reference model. We have compared our model against the LITHO1.0 model and the reference model presented by W. Shen et al. (2016), and we find significant differences in the crust and uppermost mantle. By incorporating information from previous teleseismic receiver function studies (S.-J. Chang & Baag, 2007; Y. Li et al., 2014; Ramesh et al., 2005), we find that the eastern portion of our study region requires shallower Moho depths than in LITHO1.0 and in W. Shen et al. (2016). From comparisons of forward predictions of Rayleigh wave group velocity dispersion, we find that our model can reduce

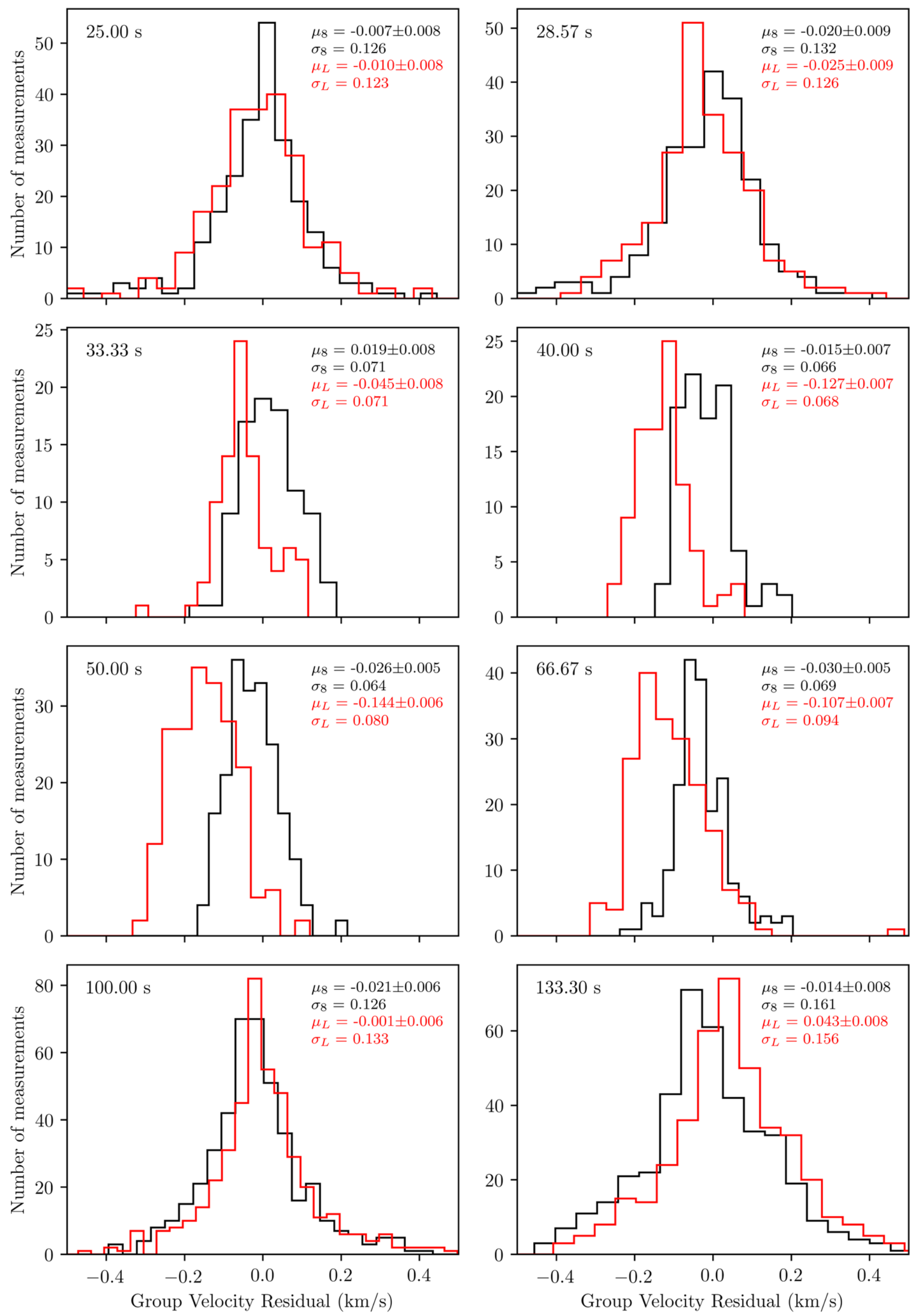

Figure 12. Histograms showing earthquake group velocity misfits. Histograms in black are for the eight-cluster model, while red histograms are for the LITHO1.0 model. Periods for each histogram are shown in the top left corners. The mean and standard deviation of each histogram is shown in the top right, where a subscript of 8 refers to the eight-cluster model and *L* refers to the LITHO1.0 model.

variance by roughly 50% with respect to LITHO1.0, with up to 90% variance reduction along certain paths. The high-velocity lithosphere east of the Ordos and Yangtze cratons in LITHO1.0 should be replaced with a broad region with a negative velocity gradient. Our 3-D *S* velocity results show the major tectonic provinces in this region, from basins at the surface such as the Ulleung, Sichuan, Songliao, and Ordos basins, to the Yangtze and Ordos cratons in the mantle, and we have also observed low-velocity regions beneath the East Sea, while along its flanks we observe high velocities just below the Moho. Persistent low-velocity regions in the mantle down to 200 km depth along the eastern margin of our model show that the cluster analysis was able to distinguish a large zone of lithospheric deformation. Overall, we show that incorporating cluster analysis in surface wave tomography studies captures the principal, large-scale variations in the study region. The individual cluster models as well as our smooth 3-D model are intended to be used as, or added to, an evolving ensemble of reference models for future local and regional geophysical investigations, such as thermochemical and geodynamic interpretations, focused tomographic studies of deeper mantle structure and dynamics, locating and characterizing local and regional seismic events, predictions of seismic wave propagation, and explanations of observations such as gravity anomalies, seismicity, and large-scale geological processes.

Acknowledgments

The revised Moho model and the *S* velocity model we present in this paper is available for download at http://geophysics.earth.northwestern.edu/seismology/EA17/. The authors would like to thank Barbara Romanowicz and an anonymous reviewer for their comments that helped to improve this paper. We are grateful for the rich variety of sources that funded this research, including a Fulbright research award to M. Witek. T.-S. Kang was funded by the Korea Meteorological Administration Research and Development Program under grant KMIPA 2015-7120. S.-J. Chang was supported by the Korea Meteorological Administration Research and Development Program under grant KMI2018-09312. The primary data processing of China Earthquake Administration related data was done by S. Ning, and the data are found at http://www.cea-igp.ac.cn. J. Ning was supported by the National Natural Science Foundation of China under grant 41374047. F-net data are obtainable from the National Research Institute for Earth Science and Disaster Prevention in Japan (http://www.fnet.bosai.go.jp). New China Digital Seismograph Network and Northeast China Extended Seismic Array data are available through the facilities of the IRIS Data Management System (http://ds.iris.edu/ds/nodes/dmc/data). Dispersion curves and data for Korean stations are referenced from Witek et al. (2014) and are available at the Korea Meteorological Administration (http://www.kma.go.kr) and the Korea Institute of Geoscience and Mineral Resources (http://www.kigam.re.kr). M. Witek, S. Ning, and S. van der Lee also acknowledge National Science Foundation grant NSF-EAR 0847951 for computational facilities, and we thank Sue Griesbach and Bob Langan for donating dedicated GPU workstations. Figures containing maps were produced using the Generic Mapping Tools (Wessel et al., 2013). To display the 3-D *S* velocity model, we use perceptually uniform colormaps developed by (Kovesi, 2015).

References

Acton, C. E., Priestley, K., Gaur, V. K., & Rai, S. S. (2010). Group velocity tomography of the indo-Eurasian collision zone. *Journal of Geophysical Research*, *115*, B12335. https://doi.org/10.1029/2009JB007021

Aki, K. (1957). Space and time spectra of stationary stochastic waves, with special reference to microtremors. *Bulletin of the Earthquake Research Institute*, *35*, 415–456.

Aminzadeh, F., & Chatterjee, S. (1984). Applications of clustering in exploration seismology. *Geoexploration*, *23*(1), 147–159. https://doi.org/10.1016/0016-7142(84)90028-0

Asamori, K., & Zhao, D. (2015). Teleseismic shear wave tomography of the Japan subduction zone. *Geophysical Journal International*, *203*(3), 1752–1772. https://doi.org/10.1093/gji/ggv334

Auger, F., & Flandrin, P. (1995). Improving the readability of time-frequency and time-scale representations by the reassignment method. *IEEE Transactions on Signal Processing*, *43*(5), 1068–1089. https://doi.org/10.1109/78.382394

Bird, P., & Toksöz, M. N. (1977). Strong attenuation of Rayleigh waves in Tibet. *Nature*, *266*(5598), 161–163. https://doi.org/10.1038/266161a0

Brocher, T. M. (2005). Empirical relations between elastic wavespeeds and density in the Earth's crust. *Bulletin of the Seismological Society of America*, *95*(6), 2018–2092. https://doi.org/10.1785/0120050077

Cara, M. (1973). Filtering of dispersed wavetrains. *Geophysical Journal International*, *33*(1), 65–80. https://doi.org/10.1111/j.1365-246X.1973.tb03415.x

Chang, S.-J., & Baag, C.-E. (2007). Moho depth and crustal VP/VS variation in southern Korea from teleseismic receiver functions: Implication for tectonic affinity between the Korean peninsula and China. *Bulletin of the Seismological Society of America*, *97*(5), 1621–1631. https://doi.org/10.1785/0120050264

Chang, K.-H., & Zhao, X. (2012). North and south China suturing in the east end: What happened in Korean Peninsula? *Gondwana Research*, *22*(2), 493–506. https://doi.org/10.1046/j.1365-246X.1999.00944.x

Chen, W.-P., & Molnar, P. (1981). Constraints on the seismic wave velocity structure beneath the Tibetan Plateau and their tectonic implications. *Journal of Geophysical Research*, *86*(B7), 5937–5962. https://doi.org/10.1029/JB086ib07p05937

Cho, K. H., Herrmann, R. B., Ammon, C. J., & Lee, K. (2007). Imaging the upper crust of the Korean Peninsula by surface-wave tomography. *Bulletin of the Seismological Society of America*, *97*(1B), 198–207. https://doi.org/10.1785/0120060096

Choi, J., Kang, T.-S., & Baag, C.-E. (2009). Three-dimensional surface wave tomography for the upper crustal velocity structure of southern Korea using seismic noise correlations. *Geosciences Journal*, *13*(4), 423–432. https://doi.org/10.1007/s12303-009-0040-2

Chough, S. K., & Barg, E. (1987). Tectonic history of Ulleung basin margin, East Sea (Sea of Japan). *Geology*, *15*(1), 45. https://doi.org/10.1130/0091-7613(1987)15<45:thoubm>2.0.co;2

Curtis, A., Trampert, J., Snieder, R., & Dost, B. (1998). Eurasian fundamental mode surface wave phase velocities and their relationship with tectonic structures. *Journal of Geophysical Research*, *103*(B11), 26,919–26,947. https://doi.org/10.1029/98JB00903

Dahlen, F. A., & Tromp, J. (1998). *Theoretical Global Seismology*. Princeton, NJ: Princeton University Press.

Davis, S. D., & Frohlich, C. (1991). Single-link cluster analysis of earthquake aftershocks: Decay laws and regional variations. *Journal of Geophysical Research*, *96*(B4), 6335–6350. https://doi.org/10.1029/90JB02634

DeMets, C., Gordon, R. G., & Argus, D. F. (2010). Geologically current plate motions. *Geophysical Journal International*, *181*(1), 1–80. https://doi.org/10.1111/j.1365-246X.2009.04491.x

Dziewonski, A., Bloch, S., & Landisman, M. (1969). A technique for the analysis of transient seismic signals. *Bulletin of the seismological Society of America*, *59*(1), 427–444.

Ekström, G., Abers, G. A., & Webb, S. C. (2009). Determination of surface-wave phase velocities across USArray from noise and Aki's spectral formulation. *Geophysical Research Letters*, *36*, L18301. https://doi.org/10.1029/2009GL039131

Fang, L., Wu, J., Ding, Z., & Panza, G. F. (2010). High resolution Rayleigh wave group velocity tomography in North China from ambient seismic noise. *Geophysical Journal International*, *181*(2), 1171–1182. https://doi.org/10.1111/j.1365-246X.2010.04571.x

Feng, M., & An, M. (2010). Lithospheric structure of the Chinese mainland determined from joint inversion of regional and teleseismic Rayleigh-wave group velocities. *Journal of Geophysical Research*, *115*, B06317. https://doi.org/10.1029/2008JB005787

Fong, D. C.-L., & Saunders, M. (2011). LSMR: An iterative algorithm for sparse least-squares problems. *SIAM Journal on Scientific Computing*, *33*(5), 2950–2971. https://doi.org/10.1137/10079687x

Gao, S., Rudnick, R. L., Carlson, R. W., McDonough, W. F., & Liu, Y.-S. (2002). Re–Os evidence for replacement of ancient mantle lithosphere beneath the North China craton. *Earth and Planetary Science Letters*, *198*(3-4), 307–322. https://doi.org/10.1016/s0012-821x(02)00489-2

Gupta, H. K., & Narain, H. (1967). Crustal structure in the Himalayan and Tibet Plateau region from surface wave dispersion. *Bulletin of the Seismological Society of America*, *57*(2), 235–248.

Holland, P. W., & Welsch, R. E. (1977). Robust regression using iteratively reweighted least-squares. *Communications in Statistics—Theory and Methods*, *6*(9), 813–827. https://doi.org/10.1080/03610927708827533

Hong, T.-K., & Kang, T.-S. (2009). Pn travel-time tomography of the paleo-continental-collision and rifting zone around Korea and Japan. *Bulletin of the Seismological Society of America*, *99*(1), 416–421. https://doi.org/10.1785/0120080120

Houser, C., Masters, G., Shearer, P., & Laske, G. (2008). Shear and compressional velocity models of the mantle from cluster analysis of long-period waveforms. *Geophysical Journal International*, *174*(1), 195–212. https://doi.org/10.1111/j.1365-246X.2008.03763.x

Hu, S., O'Sullivan, P. B., Raza, A., & Kohn, B. P. (2001). Thermal history and tectonic subsidence of the Bohai Basin, northern China: A Cenozoic rifted and local pull-apart basin. *Physics of the Earth and Planetary Interiors*, *126*(3-4), 221–235. https://doi.org/10.1016/s0031-9201(01)00257-6

Huang, Z., Li, H., Zheng, Y., & Peng, Y. (2009). The lithosphere of North China Craton from surface wave tomography. *Earth and Planetary Science Letters*, *288*(1-2), 164–173. https://doi.org/10.1016/j.epsl.2009.09.019

Huang, Z., Su, W., Peng, Y., Zheng, Y., & Li, H. (2003). Rayleigh wave tomography of China and adjacent regions. *Journal of Geophysical Research*, *108*(B2), 2073. https://doi.org/10.1029/2001JB001696

Huang, Z., Zhao, D., Hasegawa, A., Umino, N., Park, J.-H., & Kang, I.-B. (2013). Aseismic deep subduction of the Philippine sea plate and slab window. *Journal of Asian Earth Sciences*, *75*, 82–94. https://doi.org/10.1016/j.jseaes.2013.07.002

Ishiyama, T., Sato, H., Kato, N., Koshiya, S., Abe, S., Shiraishi, K., & Matsubara, M. (2017). Structures and active tectonics of compressionally reactivated back-arc failed rift across the Toyama trough in the Sea of Japan, revealed by multiscale seismic profiling. *Tectonophysics*, *710-711*, 21–36. https://doi.org/10.1016/j.tecto.2016.09.029

Jiang, C., Yang, Y., & Zheng, Y. (2014). Penetration of mid-crustal low velocity zone across the Kunlun Fault in the NE Tibetan plateau revealed by ambient noise tomography. *Earth and Planetary Science Letters*, *406*, 81–92. https://doi.org/10.1016/j.epsl.2014.08.040

Jobert, N., Journet, B., Jobert, G., Hirn, A., & Ke Zhong, S. (1985). Deep structure of southern Tibet inferred from the dispersion of Rayleigh waves through a long-period seismic network. *Nature*, *313*(6001), 386–388. https://doi.org/10.1038/313386a0

Jolivet, L., Shibuya, H., & Fournier, M. (1995). Paleomagnetic rotations and the Japan Sea opening. In B. Taylor & J. Natland (Eds.), *Active Margins and Marginal Basins of the Western Pacific* (pp. 355–369). Washington, DC: American Geophysical Union. https://doi.org/10.1029/GM088p0355

Kang, T.-S., & Shin, J. S. (2006). Surface-wave tomography from ambient seismic noise of accelerograph networks in southern Korea. *Geophysical Research Letters*, *33*, L17303. https://doi.org/10.1029/2006GL027044

Kano, K., Uto, K., & Ohguchi, T. (2007). Stratigraphic review of Eocene to Oligocene successions along the eastern Japan Sea: Implication for early opening of the Japan Sea. *Journal of Asian Earth Sciences*, *30*(1), 20–32. https://doi.org/10.1016/j.jseaes.2006.07.003

Kennett, B. L. N., Engdahl, E. R., & Buland, R. (1995). Constraints on seismic velocities in the Earth from traveltimes. *Geophysical Journal International*, *122*(1), 108–124. https://doi.org/10.1111/j.1365-246X.1995.tb03540.x

Kim, G. B., & Yoon, S.-H. (2017). An insight into asymmetric back-arc extension: Tecto-magmatic evidences from the Ulleung basin, the East Sea (Sea of Japan). *Tectonophysics*, *717*, 182–192. https://doi.org/10.1016/j.tecto.2017.07.016

Kind, R., Ni, J., Zhao, W., Wu, J., Yuan, X., Zhao, L., et al. (1996). Evidence from earthquake data for a partially molten crustal layer in southern Tibet. *Science*, *274*(5293), 1692–1694. https://doi.org/10.1126/science.274.5293.1692

Kodera, K., De Villedary, C., & Gendrin, R. (1976). A new method for the numerical analysis of non-stationary signals. *Physics of the Earth and Planetary Interiors*, *12*(2-3), 142–150. https://doi.org/10.1016/0031-9201(76)90044-3

Kovesi, P. (2015). Good colour maps: How to design them. CoRR, abs/1509.03700.

Kusky, T. M., & Li, J. (2003). Paleoproterozoic tectonic evolution of the North China Craton. *Journal of Asian Earth Sciences*, *22*(4), 383–397. https://doi.org/10.1016/s1367-9120(03)00071-3

Kwon, S., Sajeev, K., Mitra, G., Park, Y., Kim, S. W., & Ryu, I.-C. (2009). Evidence for permo-Triassic collision in far east Asia: The Korean collisional orogen. *Earth and Planetary Science Letters*, *279*(3-4), 340–349. https://doi.org/10.1016/j.epsl.2009.01.016

Lallemand, S., & Jolivet, L. (1986). Japan Sea: A pull-apart basin? *Earth and Planetary Science Letters*, *76*(3-4), 375–389. https://doi.org/10.1016/0012-821X(86)90088-9

Lebedev, S., & Nolet, G. (2003). Upper mantle beneath Southeast Asia from *S* velocity tomography. *Journal of Geophysical Research*, *108*(B1), 2048. https://doi.org/10.1029/2000JB000073

Lee, S. R., Cho, M., Yi, K., & Stern, R. A. (2000). Early Proterozoic granulites in central Korea: Tectonic correlation with Chinese cratons. *The Journal of Geology*, *108*(6), 729–738. https://doi.org/10.1086/317951

Legendre, C. P., Deschamps, F., Zhao, L., Lebedev, S., & Chen, Q.-F. (2014). Anisotropic Rayleigh wave phase velocity maps of eastern China. *Journal of Geophysical Research: Solid Earth*, *119*, 4802–4820. https://doi.org/10.1002/2013JB010781

Lekic, V., Cottaar, S., Dziewonski, A., & Romanowicz, B. (2012). Cluster analysis of global lower mantle tomography: A new class of structure and implications for chemical heterogeneity. *Earth and Planetary Science Letters*, *357-358*, 68–77. https://doi.org/10.1016/j.epsl.2012.09.014

Lekic, V., & Romanowicz, B. (2011). Tectonic regionalization without a priori information: A cluster analysis of upper mantle tomography. *Earth and Planetary Science Letters*, *308*(1-2), 151–160. https://doi.org/10.1016/j.epsl.2011.05.050

Levshin, A. L., Pisarenko, V. F., & Pogrebinsky, G. A. (1972). Frequency-time analysis of oscillations. *Annales de Geophysique*, *28*(2), 211–218.

Levshin, A. L., Ratnikova, L., & Berger, J. (1992). Peculiarities of surface-wave propagation across central Eurasia. *Bulletin of the Seismological Society of America*, *82*(6), 2464–2493.

Li, Y., Gao, M., & Wu, Q. (2014). Crustal thickness map of the Chinese mainland from teleseismic receiver functions. *Tectonophysics*, *611*, 51–60. https://doi.org/10.1016/j.tecto.2013.11.019

Li, H., Su, W., Wang, C.-Y., & Huang, Z. (2009). Ambient noise Rayleigh wave tomography in western Sichuan and eastern Tibet. *Earth and Planetary Science Letters*, *282*(1-4), 201–211. https://doi.org/10.1016/j.epsl.2009.03.021

Li, C., & van der Hilst, R. D. (2010). Structure of the upper mantle and transition zone beneath Southeast Asia from traveltime tomography. *Journal of Geophysical Research*, *115*, B07308. https://doi.org/10.1029/2009JB006882

Liang, C., & Song, X. (2006). A low velocity belt beneath northern and eastern Tibetan Plateau from Pn tomography. *Geophysical Research Letters*, *33*, L22306. https://doi.org/10.1029/2006GL027926

Lin, G., Shearer, P. M., & Hauksson, E. (2007). Applying a three-dimensional velocity model, waveform cross correlation, and cluster analysis to locate southern California seismicity from 1981 to 2005. *Journal of Geophysical Research*, *112*, B12309. https://doi.org/10.1029/2007JB004986

Lobkis, O. I., & Weaver, R. L. (2001). On the emergence of the Green's function in the correlations of a diffuse field. *The Journal of the Acoustical Society of America*, *110*(6), 3011–3017. https://doi.org/10.1121/1.1417528

Ma, Z., & Masters, G. (2014). A new global Rayleigh- and Love-wave group velocity dataset for constraining lithosphere properties. *Bulletin of the Seismological Society of America*, *104*(4), 2007–2026. https://doi.org/10.1785/0120130320

Ma, Z., Masters, G., Laske, G., & Pasyanos, M. (2014). A comprehensive dispersion model of surface wave phase and group velocity for the globe. *Geophysical Journal International*, *199*(1), 113–135. https://doi.org/10.1093/gji/ggu246

Maruyama, S., & Seno, T. (1986). Orogeny and relative plate motions: Example of the Japanese Islands. *Tectonophysics*, *127*(3-4), 305–329. https://doi.org/10.1016/0040-1951(86)90067-3

Massy, W. F. (1965). Principal components regression in exploratory statistical research. *Journal of the American Statistical Association*, *60*(309), 234–256. https://doi.org/10.1080/01621459.1965.10480787

Matsubara, Y., & Seno, T. (1980). Paleogeographic reconstruction of the Philippine Sea at 5 my bp. *Earth and Planetary Science Letters*, *51*(2), 406–414. https://doi.org/10.1016/0012-821X(80)90220-4

Menzies, M. A., Fan, W., & Zhang, M. (1993). Palaeozoic and Cenozoic lithoprobes and the loss of >120 km of Archaean lithosphere, sino-Korean craton, China, Geological Society, London. *Special Publications*, *76*(1), 71–81. https://doi.org/10.1144/gsl.sp.1993.076.01.04

Menzies, M., Xu, Y., Zhang, H., & Fan, W. (2007). Integration of geology, geophysics and geochemistry: A key to understanding the North China Craton. *Lithos*, *96*(1-2), 1–21. https://doi.org/10.1016/j.lithos.2006.09.008

Metcalfe, I. (2006). Palaeozoic and Mesozoic tectonic evolution and palaeogeography of East Asian crustal fragments: The Korean Peninsula in context. *Gondwana Research*, *9*(1-2), 24–46. https://doi.org/10.1016/j.gr.2005.04.002

Mikhailov, V., Galdeano, A., Diament, M., Gvishiani, A., Agayan, S., Bogoutdinov, S., et al. (2003). Application of artificial intelligence for Euler solutions clustering. *Geophysics*, *68*(1), 168–180. https://doi.org/10.1190/1.1543204

Miller, J. N. (1993). Tutorial review—Outliers in experimental data and their treatment. *Analyst*, *118*(5), 455–461. https://doi.org/10.1039/an9931800455

Nakajima, J., Hirose, F., & Hasegawa, A. (2009). Seismotectonics beneath the Tokyo metropolitan area, Japan: Effect of slab-slab contact and overlap on seismicity. *Journal of Geophysical Research*, *114*, B08309. https://doi.org/10.1029/2008JB006101

Nelson, K. D., Zhao, W., Brown, L. D., Kuo, J., Che, J., Liu, X., et al. (1996). Partially molten middle crust beneath southern Tibet: Synthesis of project INDEPTH results. *Science*, *274*(5293), 1684–1688. https://doi.org/10.1126/science.274.5293.1684

Nohda, S. (2009). Formation of the Japan Sea Basin: Reassessment from Ar–Ar ages and Nd–Sr isotopic data of basement basalts of the Japan Sea and adjacent regions. *Journal of Asian Earth Sciences*, *34*(5), 599–609. https://doi.org/10.1016/j.jseaes.2008.08.003

Nolet, G. (1990). Partitioned waveform inversion and two-dimensional structure under the network of autonomously recording seismographs. *Journal of Geophysical Research*, *95*(B6), 8499. https://doi.org/10.1029/JB095ib06p08499

Northrup, C., Royden, L., & Burchfiel, B. (1995). Motion of the Pacific plate relative to Eurasia and its potential relation to Cenozoic extension along the eastern margin of Eurasia. *Geology*, *23*(8), 719–722. https://doi.org/10.1130/0091-7613(1995)023<0719:MOTPPR>2.3.CO;2

Otofuji, Y.-I., Itaya, T., & Matsuda, T. (1991). Rapid rotation of southwest Japan—palaeomagnetism and K-Ar ages of Miocene volcanic rocks of southwest Japan. *Geophysical Journal International*, *105*(2), 397–405. https://doi.org/10.1111/j.1365-246X.1991.tb06721.x

Otofuji, Y.-I., Matsuda, T., & Nohda, S. (1985). Opening mode of the Japan Sea inferred from the palaeomagnetism of the Japan Arc. *Nature*, *317*(6038), 603–604. https://doi.org/10.1038/317603a0

Paige, C. C., & Saunders, M. A. (1982). LSQR: An algorithm for sparse linear equations and sparse least squares. *ACM Transactions on Mathematical Software*, *8*(1), 43–71. https://doi.org/10.1145/355984.355989

Pasyanos, M. E., Masters, T. G., Laske, G., & Ma, Z. (2014). LITHO1.0: An updated crust and lithospheric model of the Earth. *Journal of Geophysical Research: Solid Earth*, *119*, 2153–2173. https://doi.org/10.1002/2013JB010626

Pedersen, H. A., Mars, J. I., & Amblard, P. (2003). Improving surface–wave group velocity measurements by energy reassignment. *Geophysics*, *68*(2), 677–684. https://doi.org/10.1190/1.1567238

Pines, I., Teng, T.-L., Rosenthal, R., & Alexander, S. (1980). A surface wave dispersion study of the crustal and upper mantle structure of China. *Journal of Geophysical Research*, *85*(B7), 3829–3844. https://doi.org/10.1029/JB085ib07p03829

Ramesh, D. S., Kawakatsu, H., Watada, S., & Yuan, X. (2005). Receiver function images of the central Chugoku region in the Japanese islands using Hi-net data. *Earth Planet Sp*, *57*(4), 271–280. https://doi.org/10.1186/bf03352563

Ree, J.-H., Cho, M., Kwon, S.-T., & Nakamura, E. (1996). Possible eastward extension of Chinese collision belt in South Korea: The Imjingang belt. *Geology*, *24*(12), 1071–1074. https://doi.org/10.1130/0091-7613(1996)024<1071:peeocc>2.3.co;2

Rihaczek, A. (1968). Signal energy distribution in time and frequency. *IEEE Transactions on Information Theory*, *14*(3), 369–374. https://doi.org/10.1109/tit.1968.1054157

Ritzwoller, M. H., & Levshin, A. L. (1998). Eurasian surface wave tomography: Group velocities. *Journal of Geophysical Research*, *103*(B3), 4839–4878. https://doi.org/10.1029/97JB02622

Rodi, W. L., Glover, P., Li, T. M. C., & Alexander, S. S. (1975). A fast, accurate method for computing group-velocity partial derivatives for Rayleigh and Love modes. *Bulletin of the Seismological Society of America*, *65*(5), 1105–1114.

Romanowicz, B. A. (1982). Constraints on the structure of the Tibet Plateau from pure path phase velocities of Love and Rayleigh waves. *Journal of Geophysical Research*, *87*(B8), 6865–6883. https://doi.org/10.1029/JB087ib08p06865

Schmid, C., van der Lee, S., & Giardini, D. (2006). Correlated shear and bulk moduli to 1400 km beneath the Mediterranean region. *Physics of the Earth and Planetary Interiors*, *159*(3-4), 213–224. https://doi.org/10.1016/j.pepi.2006.07.003

Schmid, C., van der Lee, S., VanDecar, J. C., Engdahl, E. R., & Giardini, D. (2008). Three-dimensional *S* velocity of the mantle in the Africa-Eurasia plate boundary region from phase arrival times and regional waveforms. *Journal of Geophysical Research*, *113*, B03306. https://doi.org/10.1029/2005JB004193

Seno, T., & Maruyama, S. (1984). Paleogeographic reconstruction and origin of the Philippine Sea. *Tectonophysics*, *102*(1-4), 53–84. https://doi.org/10.1016/0040-1951(84)90008-8

Shapiro, N. M. (2005). High-resolution surface-wave tomography from ambient seismic noise. *Science*, *307*(5715), 1615–1618. https://doi.org/10.1126/science.1108339

Shapiro, N. M., & Ritzwoller, M. H. (2002). Monte-Carlo inversion for a global shear-velocity model of the crust and upper mantle. *Geophysical Journal International*, *151*(1), 88–105. https://doi.org/10.1046/j.1365-246X.2002.01742.x

Shearer, P. (2005). Southern California hypocenter relocation with waveform cross correlation, part 2: Results using source-specific station terms and cluster analysis. *Bulletin of the Seismological Society of America*, *95*(3), 904–915. https://doi.org/10.1785/0120040168

Shen, Y., Ren, Y., Gao, H., & Savage, B. (2012). An improved method to extract very-broadband empirical Green's functions from ambient seismic noise. *Bulletin of the Seismological Society of America*, *102*(4), 1872–1877. https://doi.org/10.1785/0120120023

Shen, W., Ritzwoller, M., Kang, D., Kim, Y., Lin, F. C., Ning, J., et al. (2016). A seismic reference model for the crust and uppermost mantle beneath China from surface wave dispersion. *Geophysical Journal International*, *206*(2), 954–979. https://doi.org/10.1093/gji/ggw175

Tian, Z.-Y., Han, P., & Xu, K.-D. (1992). The Mesozoic-Cenozoic East China rift system. *Tectonophysics*, *208*(1-3), 341–363. https://doi.org/10.1016/0040-1951(92)90354-9

Van Horne, A., Sato, H., & Ishiyama, T. (2017). Evolution of the Sea of Japan back-arc and some unsolved issues. *Tectonophysics*, *710*, 6–20. https://doi.org/10.1016/j.tecto.2016.08.020

van der Lee, S., & Nolet, G. (1997). Upper mantle *S* velocity structure of North America. *Journal of Geophysical Research*, *102*(B10), 22,815–22,838. https://doi.org/10.1029/97JB01168

Vasco, D. W., Peterson, J. E., & Majer, E. L. (1996). Nonuniqueness in traveltime tomography: Ensemble inference and cluster analysis. *Geophysics*, *61*(4), 1209–1227. https://doi.org/10.1190/1.1444040

Villaseõr, A., Ritzwoller, M., Levshin, A., Barmin, M., Engdahl, E., Spakman, W., & Trampert, J. (2001). Shear velocity structure of central Eurasia from inversion of surface wave velocities. *Physics of the Earth and Planetary Interiors*, *123*(2-4), 169–184. https://doi.org/10.1016/s0031-9201(00)00208-9

Wang, Z., & Dahlen, F. A. (1995). Spherical-spline parameterization of three-dimensional Earth models. *Geophysical Research Letters*, *22*(22), 3099–3102. https://doi.org/10.1029/95GL03080

Wang, Y., Fan, W., Cawood, P. A., & Li, S. (2008). Sr–Nd–Pb isotopic constraints on multiple mantle domains for Mesozoic mafic rocks beneath the South China Block hinterland. *Lithos*, *106*(3-4), 297–308. https://doi.org/10.1016/j.lithos.2008.07.019

Ward, J. H. (1963). Hierarchical grouping to optimize an objective function. *Journal of the American Statistical Association*, *58*(301), 236–244. https://doi.org/10.1080/01621459.1963.10500845

Wei, W. (2001). Detection of widespread fluids in the Tibetan crust by magnetotelluric studies. *Science*, *292*(5517), 716–719. https://doi.org/10.1126/science.1010580

Wessel, P., Smith, W. H. F., Scharroo, R., Joachum, L., & Wobbe, F. (2013). Generic Mapping Tools: Improved version released. *Eos, Transactions of the American Geophysical Union*, *94*(45), 409–410. https://doi.org/10.1002/2013EO450001

White, R., & McKenzie, D. (1989). Magmatism at rift zones: The generation of volcanic continental margins and flood basalts. *Journal of Geophysical Research*, *94*(B6), 7685. https://doi.org/10.1029/JB094ib06p07685

Witek, M., van der Lee, S., & Kang, T.-S. (2014). Rayleigh wave group velocity distributions for East Asia using ambient seismic noise. *Geophysical Research Letters*, *41*, 8045–8052. https://doi.org/10.1002/2014GL062016

Wu, Y.-B., Gao, S., Gong, H.-J., Xiang, H., Jiao, W.-F., Yang, S.-H., et al. (2009). Zircon U-Pb age, trace element and Hf isotope composition of Kongling terrane in the Yangtze Craton: Refining the timing of Palaeoproterozoic high-grade metamorphism. *Journal of Metamorphic Geology*, *27*(6), 461–477. https://doi.org/10.1111/j.1525-1314.2009.00826.x

Wu, Y., Gao, S., Zhang, H., Zheng, J., Liu, X., Wang, H., et al. (2012). Geochemistry and zircon U–Pb geochronology of paleoproterozoic arc related granitoid in the northwestern Yangtze block and its geological implications. *Precambrian Research*, *200-203*, 26–37. https://doi.org/10.1016/j.precamres.2011.12.015

Wu, F. T., Levshin, A. L., & Kozhevnikov, V. M. (1997). Rayleigh wave group velocity tomography of Siberia, China and the vicinity. *Pure and Applied Geophysics*, *149*(3), 447–473. https://doi.org/10.1007/s000240050035

Wu, F., Lin, J., Wilde, S., Zhang, X., & Yang, J. (2005). Nature and significance of the early Cretaceous giant igneous event in eastern China. *Earth and Planetary Science Letters*, *233*(1-2), 103–119. https://doi.org/10.1016/j.epsl.2005.02.019

Wu, F.-Y., Walker, R. J., Ren, X.-W., Sun, D.-Y., & Zhou, X.-H. (2003). Osmium isotopic constraints on the age of lithospheric mantle beneath northeastern China. *Chemical Geology*, *196*(1-4), 107–129. https://doi.org/10.1016/s0009-2541(02)00409-6

Xu, Y.-G. (2001). Thermo-tectonic destruction of the Archaean lithospheric keel beneath the Sino-Korean craton in China: Evidence, timing and mechanism. *Physics and Chemistry of the Earth, Part A: Solid Earth and Geodesy*, *26*(9-10), 747–757. https://doi.org/10.1016/s1464-1895(01)00124-7

Xu, Z., Zhao, Z.-F., & Zheng, Y.-F. (2012). Slab–mantle interaction for thinning of cratonic lithospheric mantle in North China: Geochemical evidence from Cenozoic continental basalts in central Shandong. *Lithos*, *146*, 202–217. https://doi.org/10.1016/j.lithos.2012.05.019

Yang, Y., Ritzwoller, M. H., Zheng, Y., Shen, W., Levshin, A. L., & Xie, Z. (2012). A synoptic view of the distribution and connectivity of the mid-crustal low velocity zone beneath Tibet. *Journal of Geophysical Research*, *117*, B04303. https://doi.org/10.1029/2011JB008810

Yang, Y., Zheng, Y., Chen, J., Zhou, S., Celyan, S., Sandvol, E., et al. (2010). Rayleigh wave phase velocity maps of Tibet and the surrounding regions from ambient seismic noise tomography. *Geochemistry, Geophysics, Geosystems*, *11*, Q08010. https://doi.org/10.1029/2010GC003119

Yao, H., Beghein, C., & van der Hilst, R. D. (2008). Surface wave array tomography in SE Tibet from ambient seismic noise and two-station analysis—II. crustal and upper-mantle structure. *Geophysical Journal International*, *173*(1), 205–219. https://doi.org/10.1111/j.1365-246X.2007.03696.x

Yao, H., & van der Hilst, R. D. (2009). Analysis of ambient noise energy distribution and phase velocity bias in ambient noise tomography, with application to SE Tibet. *Geophysical Journal International*, *179*(2), 1113–1132. https://doi.org/10.1111/j.1365-246X.2009.04329.x

Yao, H., van der Hilst, R. D., & de Hoop, M. V. (2006). Surface-wave array tomography in SE Tibet from ambient seismic noise and two-station analysis—I. phase velocity maps. *Geophysical Journal International*, *166*(2), 732–744. https://doi.org/10.1111/j.1365-246X.2006.03028.x

Ye, H., Shedlock, K. M., Hellinger, S. J., & Sclater, J. G. (1985). The North China Basin: An example of a Cenozoic rifted intraplate basin. *Tectonics*, *4*(2), 153–169. https://doi.org/10.1029/TC004i002p00153

Yu, J.-H., O'Reilly, S. Y., Zhou, M.-F., Griffin, W., & Wang, L. (2012). U–Pb geochronology and Hf–Nd isotopic geochemistry of the Badu complex, southeastern China: Implications for the Precambrian crustal evolution and paleogeography of the Cathaysia Block. *Precambrian Research*, *222-223*, 424–449. https://doi.org/10.1016/j.precamres.2011.07.014

Zaliapin, I., Gabrielov, A., Keilis-Borok, V., & Wong, H. (2008). Clustering analysis of seismicity and aftershock identification. *Physical Review Letters*, *101*(1), 18501. https://doi.org/10.1103/physrevlett.101.018501

Zhang, J.-J., Zheng, Y.-F., & Zhao, Z.-F. (2009). Geochemical evidence for interaction between oceanic crust and lithospheric mantle in the origin of Cenozoic continental basalts in east-central China. *Lithos*, *110*(1-4), 305–326. https://doi.org/10.1016/j.lithos.2009.01.006

Zhao, D. (2017). Big mantle wedge, anisotropy, slabs and earthquakes beneath the Japan Sea. *Physics of the Earth and Planetary Interiors*, *270*, 9–28. https://doi.org/10.1016/j.pepi.2017.06.009

Zhao, G., & Cawood, P. A. (2012). Precambrian geology of China. *Precambrian Research*, *222-223*, 13–54. https://doi.org/10.1016/j.precamres.2012.09.017

Zhao, D., & Hasegawa, A. (1993). *P*-wave tomographic imaging of the crust and upper mantle beneath the Japan Islands. *Journal of Geophysical Research*, *98*(B3), 4333–4353. https://doi.org/10.1029/92JB02295

Zhao, D., Hasegawa, A., & Kanamori, H. (1994). Deep structure of Japan subduction zone as derived from local, regional, and teleseismic events. *Journal of Geophysical Research*, *99*(B11), 22,313–22,329. https://doi.org/10.1029/94JB01149

Zhao, D., Matsuzawa, T., & Hasegawa, A. (1997). Morphology of the subducting slab boundary in the northeastern Japan arc. *Physics of the Earth and Planetary Interiors*, *102*(1-2), 89–104. https://doi.org/10.1016/s0031-9201(96)03258-x

Zhao, D., Yanada, T., Hasegawa, A., Umino, N., & Wei, W. (2012). Imaging the subducting slabs and mantle upwelling under the Japan Islands. *Geophysical Journal International*, *190*(2), 816–828. https://doi.org/10.1111/j.1365-246X.2012.05550.x

Zheng, Y., Shen, W., Zhou, L., Yang, Y., Xie, Z., & Ritzwoller, M. H. (2011). Crust and uppermost mantle beneath the North China Craton, northeastern China, and the Sea of Japan from ambient noise tomography. *Journal of Geophysical Research*, *116*, B12312. https://doi.org/10.1029/2011JB008637

Zheng, S., Sun, X., Song, X., Yang, Y., & Ritzwoller, M. H. (2008). Surface wave tomography of China from ambient seismic noise correlation. *Geochemistry, Geophysics, Geosystems*, *9*, Q05020. https://doi.org/10.1029/2008GC001981

Zheng, Y.-F., Xiao, W.-J., & Zhao, G. (2013). Introduction to tectonics of China. *Gondwana Research*, *23*(4), 1189–1206. https://doi.org/10.1016/j.gr.2012.10.001

Zheng, Y., & Zhang, S. (2007). Formation and evolution of Precambrian continental crust in South China. *Chinese Science Bulletin*, *52*(1), 1–12. https://doi.org/10.1007/s11434-007-0015-5

Zhou, L., Xie, J., Shen, W., Zheng, Y., Yang, Y., Shi, H., & Ritzwoller, M. H. (2012). The structure of the crust and uppermost mantle beneath South China from ambient noise and earthquake tomography. *Geophysical Journal International*, *189*(3), 1565–1583. https://doi.org/10.1111/j.1365-246X.2012.05423.x